AIAA SciTech Forum
11–15 & 19–21 January 2021, VIRTUAL EVENT
AIAA Scitech 2021 Forum

10.2514/6.2021-1300

Excitation Line Optimization for Krypton Tagging Velocimetry and Planar Laser-Induced Fluorescence in the 200-220 nm Range

D. Shekhtman* M. A. Mustafa† N. J. Parziale‡
Stevens Institute of Technology, Hoboken, NJ 07030, USA

Krypton tagging velocimetry (KTV) requires high signal-to-noise ratio (SNR) to observe high-speed boundary layers and flow structures. In order to optimize the choice of laser excitation line for use in KTV (212.556 nm, 214.769 nm, 216.667 nm), a theoretical and experimental investigation of excitation processes was undertaken. This paper presents a multi-path, two-photon excitation, cross-section calculation, using an assumed finite basis of states consisting of $4p$, $5s$, $6s$, $7s$, $5p$, $6p$, $4d$, $5d$, and $6d$ orbitals. From the relative magnitudes of two-photon cross-sections for five Krypton lines, an excitation spectrum is constructed and compared against excitation spectrum data, with encouraging results. From this work and the successful comparison to experiment from our lab and those in the literature, we conclude that the optimal line is 212.556 nm for Kr-PLIF and single-laser KTV. For KTV where the read step in performed with a continuous wave (CW) laser diode, the 216.667 nm write-laser excitation is optimal.

Nomenclature

c	= Speed of Light (m/s)
e	= Electron Charge, (C)
ϵ_o	= Free Space Permittivity, (C^2/(N·m^2))
h	= Planck Constant, (J·s)
$\hbar$	= Reduced Planck Constant (J·s/rad)), $\hbar = h/(2\pi)$
m_{kr}	= Mass of a Kr Atom, (kg)
m_e	= Mass of an Electron, (kg)
Z	= Atomic Number of Kr
Z_e	= Effective Nuclear Charge
α	= Fine Structure Constant, $\alpha = e^2/(4\pi\epsilon_o\hbar c)$
a_o	= Bohr Radius, (cm), $a_o = 100\hbar/(\alpha m_e c)$
d_D	= Debye Length, (m)
Ry	= Rydberg Constant, (J), $Ry = \hbar^2/(2m_e a_o^2) = (1/2)m_e\alpha^2c^2$
k_b	= Boltzmann Constant, (J/(atom·K))
r	= Radius, (Bohr Radii, a_o)
θ	= Azimuth Angle, (rad)
ϕ	= Polar Angle, (rad)
$\hat{\epsilon}$	= Polarization Unit Vector of Laser Electric Field
q	= Polarization Component
$\hat{\epsilon}\cdot\vec{r}$	= Dipole Operator, (Bohr Radius)
D	= Matrix Representation of Dipole Operator, (Bohr Radius)
G	= Matrix Representation of Green's Function Operator, (s/rad)
$M_{fg}^{(2)}$	= Two-Photon Transition Matrix Element from states $\lvert g\rangle$ to $\lvert f\rangle$, ($a_o^2\cdot$ s)

*Graduate Student, Mechanical Engineering, Castle Point on Hudson, Hoboken, New Jersey, 07030.
†Postdoctoral Student, Mechanical Engineering, Castle Point on Hudson, Hoboken, New Jersey, 07030.
‡Associate Professor, Mechanical Engineering, Castle Point on Hudson, Hoboken, New Jersey, 07030, AIAA Senior Member.

$W_{f,g}$ = Two-Photon Excitation Rate, (1/s)
W_{pi} = One-Photon Ionization Rate, (1/s)
$\sigma_o^{(2)}$ = Two-Photon Cross-section, (cm^4)
$\sigma^{(2)}$ = Two-Photon Rate-coefficient, (cm^4·s)
σ_{pi} = One-Photon Ionization Cross-section, (cm^2)
I = Laser Intensity (J/(cm^2·s))
$|k\rangle$ = Intermediate State k
$|g\rangle$ = Ground State
$|f\rangle$ = Final Two-Photon Excited State
E_k = Energy of level k, (eV)
ω_L = Angular Frequency of Laser Excitation, (rad·s^{-1})
ω_k = Angular Frequency for Intermediate Energy State k, (rad·s^{-1}), $\omega_k = E_k/\hbar$
ω_g = Angular Frequency for Ground Energy State g, (rad·s^{-1}), $\omega_g = E_g/\hbar$
ω_{ij} = Observed Angular Frequency for Transition from states i to j, (rad·s^{-1}), $\omega_{ij} = (E_i - E_j)/\hbar$
$g(2\omega_L)$ = Lineshape Function, (s)
F = Laser Photon Flux, (photon/s), $F = I/(\hbar\omega_L)$
$\hat{e}_i$ = Vector Representation of State $|i\rangle$
λ_{ij} = Transition wavelength from state i to state j, (nm)
A_{ij} = Einstein coefficient (transition probability) for transition from state i to j, (s^{-1})
n = Principal Quantum Number
n^* = Effective Principal Quantum Number
l = Angular Momentum Quantum Number
l^* = Effective Angular Momentum Quantum Number
m = Azimuth Angular Momentum Quantum Number
L = Total Orbital Angular Momentum Quantum Number for an Atom
S = Total Electron Spin Quantum Number for an Atom
J = Coupled Angular Momentum Quantum Number, $J = \left|\vec{J}\right| = \left|\vec{L} + \vec{S}\right|$
M = Azimuth Projection of $\vec{J}$
w_t = # of allowable, nonzero transitions from state $|j\rangle$ to state $|i\rangle$
δ_d = Quantum Defect
R_{nl} = Radial Wave Function
Y_l^m = Scalar Spherical Harmonic Function
$\mathbf{Y}_{JM}^{LS}$ = Spherical Harmonic Tensor Function
P = Pressure, (Pa)
V = Volume, (m^3)
T = Temperature, (K)
T_e = Electron Temperature, (K)
N_e = Number of Electrons, (electrons)
t = Time, (s)

I. Introduction

There are multiple excitation lines for the two-photon excitation of Kr in the 190-220 nm range: 192.749 nm, 193.494 nm, 193.947 nm, 202.316 nm, 204.196 nm, 212.556 nm, 214.769 nm, and 216.667 nm. The optimal choice of excitation line for krypton fluorescence experiments is subject to test requirements, such as signal-to-noise ratio (SNR), background luminosity, and, in the case of KTV, the write/read delay time. When determining the optimal scheme for krypton fluorescence experiments, evaluating the two-photon cross-section is the starting point and, as such, the motivation for the current work.

Krypton fluorescence experiments have attracted great interest over the last decade because of their promise in making fundamental contributions in subsonic and supersonic combustion in addition to supersonic and hypersonic aerodynamics.[1] Two such experiments are krypton planar laser-induced fluorescence (Kr-PLIF) and krypton tagging velocimetry (KTV). Kr-PLIF and KTV are performed by the addition of a small mole fraction of Kr to a high-speed/reacting flow. This strategy has enabled the non-intrusive measurement of important quantities such as density, temperature, mixing-fraction, and velocity that were not previously possible in difficult-to-measure gas flows.

Initial Kr-PLIF work was performed at 214.7 nm,[2–6] which now includes thermometry.[7–9] Additionally, the 204.196 nm line has also been used for Kr-PLIF.[10–12] Experimental Kr-PLIF excitation line comparisons have been performed by,[13,14] with the observation that the 212.556 nm was superior. High-speed Kr-PLIF was performed at 212.556 nm by Grib *et al.*[15] Original KTV work relied on write-line excitation at 214.769 nm to generate the metastable Kr state.[16–25] In more recent KTV work[26–28] and in this paper, we observe higher SNR for single-laser, unfiltered KTV with a 212.556 nm write-line excitation; additionally, we observe that two-photon excitation at 216.667 nm is optimal for KTV where the read step uses a laser diode.

In this paper, we calculate the two-photon cross-sections of Kr to (1) remove any ambiguity in the superiority of the 212.556 nm line for Kr-PLIF and single-laser KTV; (2) provide fundamental physical insights to verify the Richardson *et al.*[13] excitation spectrum; (3) provide reliable cross-sections for modeling other Kr excitation schemes; and (4) prepare a framework for calculating multiphoton excitation spectra for other noble gas atoms. Herein, we detail our calculation method and compare the results of those calculations to experimental results with success. Additionally, we present time- and pressure- resolved experimental data of excitation performed with a near IR laser diode, for which the 216.667 nm line KTV is optimal.

II. Krypton Tagging Velocimetry

The current state of KTV rests on $(2+1)$ resonant enhanced multiphoton ionization (REMPI) to partially ionize Kr gas and observe a long-lasting afterglow produced by electron-ion recombination and its resulting radiative cascade.[29] REMPI is a compound process consisting of two-photon excitation followed by a one-photon ionization. It is magnitudes more efficient than direct three-photon ionization.[30] In Table 1, there are multiple excitation lines for the two-photon excitation of Kr in the 190-220 nm range that are accessible with commercially available optics and laser systems. Krypton atoms can be excited to any of these levels during the write step to form the tagged tracer. This paper considers and compares the last three lines: 212.556 nm, 214.769 nm, and 216.667 nm.

Table 1: Accessible Kr levels with two-photon excitation. Racah nl[K]$_J$ notation.

λ_L (nm)	Energy Level (-)	E (cm^{-1})
192.749	6p[1/2]$_0$	103761.6336
193.494	6p[3/2]$_2$	103362.6124
193.947	6p[5/2]$_2$	103121.1419
202.316	5p′[1/2]$_0$	98855.0698
204.196	5p′[3/2]$_2$	97945.1664
212.556	5p[1/2]$_0$	94092.8626
214.769	5p[3/2]$_2$	93123.3409
216.667	5p[5/2]$_2$	92307.3786

Following the transitions in the energy level diagrams in Fig. 1 along with the relevant transition data in Table 2, the three KTV schemes are performed as follows.

1. $\lambda_L = 216.667$ nm

   Write Step: Excite krypton atoms with a pulsed tunable laser to form two tagged tracers, metastable Kr and Kr$^+$, through (2+1) photoionization. Two-photon excitation of $4p^6(^1\mathrm{S}_0) \rightarrow 5p[5/2]_2$ (216.67 nm, transition A) and subsequent one-photon ionization[31] to Kr$^+$ (216.67 nm, transition B) occur. This is followed by decay to metastable $5p[5/2]_2 \rightarrow 5s[3/2]^o_2$ (transition D) and resonance states $5p[5/2]_2 \rightarrow 5s[3/2]^o_1$ (transition C), and other transitions, J, K and L resulting from the recombination process,[32,33] I. Using a camera oriented normal to the flow, the position of the write line is recorded by gated imaging of the laser-induced-fluorescence (LIF) from transitions (C, D, J, K, L).

Read Step: After a prescribed delay, record the displacement of the tagged metastable krypton and Kr^+. With an additional tunable laser, excite $5p[3/2]_1$ level by the $5s[3/2]^o_2 \rightarrow 5p[3/2]_1$ transition (769.454 nm, E), which is followed by decay to metastable $5p[3/2]_1 \rightarrow 5s[3/2]^o_1$ (829.81 nm, G) and resonance $5p[3/2]_1 \rightarrow 5s[3/2]^o_2$ (769.454 nm, F) states. The position of the read line is marked by gated imaging of the LIF from transitions F and G and the residual fluorescence from transitions J, K and L that result from the recombination process, I.

2. $\lambda_L = 214.769$ nm

   Write Step: Excite krypton atoms with a pulsed tunable laser to form two tagged tracers, metastable Kr and Kr^+, through (2+1) photoionization. Two-photon excitation of $4p^6(^1S_0) \rightarrow 5p[5/2]_2$ (214.769 nm, transition $A^\dagger$) and subsequent one-photon ionization[31] to Kr^+ (214.769 nm, transition $B^\dagger$) occur. This is followed by decay to metastable $5p[3/2]_2 \rightarrow 5s[3/2]^o_2$ (transition N) and resonance states $5p[3/2]_2 \rightarrow 5s[3/2]^o_1$ (transition O), and other transitions, J, K and L resulting from the recombination process,[32,33] I. The position of the write line is marked by gated imaging of the LIF from these transitions (N, O, J, K, L), recorded with a camera positioned normal to the flow.

   Read Step: After a prescribed delay, record the displacement of the tagged metastable krypton and Kr^+. With an additional tunable laser, excite $5p[3/2]_1$ level by the $5s[3/2]^o_2 \rightarrow 5p[3/2]_1$ transition (769.454 nm, E), which is followed by decay to metastable $5p[3/2]_1 \rightarrow 5s[3/2]^o_1$ (829.81 nm, G) and resonance $5p[3/2]_1 \rightarrow 5s[3/2]^o_2$ (769.4547 nm, F) states. The position of the read line is marked by gated imaging of the LIF from transitions F and G and the residual fluorescence from transitions J, K and L that result from the recombination process, I.

3. $\lambda_L = 212.556$ nm

   Write Step: Excite krypton atoms with a pulsed tunable laser to form two tagged tracers, metastable Kr and Kr^+, through (2+1) photoionization. Two-photon excitation of $4p^6(^1S_0) \rightarrow 5p[1/2]_0$ (212.556 nm, transition A^*) and subsequent one-photon ionization[31] to Kr^+ (212.556 nm, transition B^*) occur. This is followed by decay to the resonance state $5p[1/2]_0 \rightarrow 5s[3/2]^o_1$ (transition M) and other transitions, J, K and L resulting from the recombination process,[32,33] I. The metastable state is formed through transition J. The position of the write line is marked by gated imaging of the LIF from these transitions (M, J, K, L), recorded with a camera positioned normal to the flow.

   Read Step: After a prescribed delay, record the displacement of the tagged metastable krypton and Kr^+. With an additional tunable laser, excite $5p[3/2]_1$ level by the $5s[3/2]^o_2 \rightarrow 5p[3/2]_1$ transition (769.454 nm, E), which is followed by decay to metastable $5p[3/2]_1 \rightarrow 5s[3/2]^o_1$ (829.81 nm, G) and resonance $5p[3/2]_1 \rightarrow 5s[3/2]^o_2$ (769.454 nm, F) states. The position of the read line is marked by gated imaging of the LIF from transitions F and G and the fluorescence from transitions J, K and L that result from the recombination process, I.

The extent of ionization in all three schemes is proportional to the intensity of the laser beam, which is limited by the available laser power and the experimental setup (ex. window transmission and laser beam splitting). Lower laser power reduces (and can effectively eliminate) ionization and its subsequent radiative cascade, which may or may not be good for tracing. At low power, fluorescence from transitions J, K and L become insignificant. At the write step, this is not an issue in the three schemes because the fluorescence from transitions C, D, N, O and M dominates that of transitions J, K and L. At the read step, the schemes behave differently. The schemes that use $\lambda_L = 214.769$ and 216.67 nm create metastable Kr through transitions D and N, which do not rely on ionization. The fluorescence from the re-excitation of the metastable state, transitions F and G is often sufficient on its own without the need for the fluorescence from transitions J, K and L. Therefore, these two schemes can be used even without ionization. However, the $\lambda_L = 212.556$ nm scheme is completely reliant on recombination processes and their resulting radiative cascade to create fluorescence at the read step. Metastable Kr in this scheme is produced though recombination, I, and subsequently, transition J. Hence, if there is no ionization, I and J do not occur. Then at the read step, there is no metastable Kr to re-excite (transitions E, F and G do not occur), and there would be no fluorescence from transitions J, K and L. Therefore, this scheme requires the Kr atoms to be ionized to form Kr^+ and metastable Kr as the tracers. Consequently, the power requirement for this scheme is higher than that of

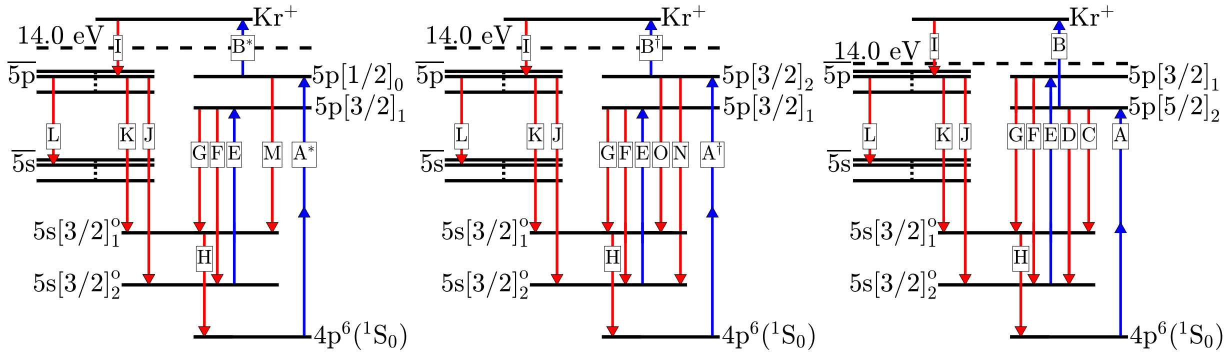

Figure 1: Energy diagrams (not to scale) with Racah nl[K]$_J$ notation for the three excitation schemes. *Left:* 212.556 nm. *Center:* 214.769 nm. *Right:* 216.667 nm. Transition details in Table 2. States $\overline{5p}$ and $\overline{5s}$ represent the numerous 5p and 5s states (tabulated in Mustafa et al.[27]) that are created by the recombination process, I. Transitions J, K and L represent the numerous transitions in the 5p-5s band. 14.0 eV marks ionization limit of Kr.

Table 2: Relevant NIST Atomic Spectra Database Lines Data, labels match Fig. 1. Racah nl[K]$_J$ notation. Transition I is not listed because it is not an atomic-level transition. It represents the recombination process. Entries in the J/K/L row represent ranges and order of magnitude estimates since J, K and L in Fig. 1 represent numerous transitions in the 5p-5s band. k and i denote the upper and lower energy levels respectively.

Transition	λ_{air} (nm)	Nature	Lower Level	Upper Level	A_{ij} (1/s)	E_j (cm^{-1})	E_i (cm^{-1})
A	216.670	Two-Photon	4s^{2}4p^6, ^{1}S$_0$	5p[5/2]$_2$	(-)	0	92307.3786
A†	214.769	Two-Photon	4s^{2}4p^6, ^{1}S$_0$	5p[3/2]$_2$	(-)	0	93123.3409
A*	212.556	Two-Photon	4s^{2}4p^6, ^{1}S$_0$	5p[1/2]$_0$	(-)	0	94092.8626
B	216.667	Single-Photon	5p[5/2]$_2$	Kr+	(-)	92307.3786	112917.62
B†	214.769	Single-Photon	5p[3/2]$_2$	Kr+	(-)	93123.3409	112917.62
B*	212.556	Single-Photon	5p[1/2]$_0$	Kr+	(-)	94092.8626	112917.62
C	877.675	Single-Photon	5s[3/2]$_1$	5p[5/2]$_2$	2.2×10^7	80916.7680	92307.3786
D	810.436	Single-Photon	5s[3/2]$_2$	5p[5/2]$_2$	8.9×10^6	79971.7417	92307.3786
E/F	769.454	Single-Photon	5s[3/2]$_2$	5p[3/2]$_1$	4.3×10^6	79971.7417	92964.3943
G	829.811	Single-Photon	5s[3/2]$_1$	5p[3/2]$_1$	2.9×10^7	80916.7680	92964.3943
H	123.584	Single-Photon	4s^{2}4p^6, ^{1}S$_0$	5s[3/2]$_1$	3.0×10^8	0	80916.7680
J/K/L	750-830	Single-Photon	$\overline{5s}$	$\overline{5p}$	10^6-10^7	80000.0000	90000.0000
M	758.950	Single-Photon	5s[3/2]$_1$	5p[1/2]$_0$	4.31×10^7	80916.7680	94092.8626
N	760.364	Single-Photon	5s[3/2]$_2$	5p[3/2]$_2$	2.732×10^7	79971.7417	93123.3409
O	819.230	Single-Photon	5s[3/2]$_1$	5p[3/2]$_2$	1.1×10^7	80916.7680	93123.3409

the other two.

A simplified version of KTV that utilizes only a write laser[26,27] can also be implemented by omitting the read laser and its re-excitation of the metastable state (transition E). Therefore, in all three schemes, the fluorescence imaged at the read step is generated solely from transitions J, K and L. As mentioned earlier, transitions J, K and L result from the radiative cascade of a cold Kr plasma. While the use of only one laser offers significant reductions in cost and experimental complexity, the use of a single laser necessitates high laser power, sufficient to ionize krypton atoms.

Fig. 2 shows the time resolved fluorescence signal from schemes that utilize $\lambda_L = 212.556$ and 214.769 nm. This data is from the single-laser version of an excitation scheme with no read laser, and was taken in a 99% N_2/1% Kr gas mixture at 5 torr. The yellow region in the graph indicates the camera gate at the write step, which is typically a 5 ns exposure. The two green regions are indicative of the camera gate at the read step with a 500 (left) and 1000 (right) ns delay, and a 50 ns exposure. The results show that the signal-to-noise ratio, SNR, of the 212.556 nm scheme is higher relative to the 214.769 nm scheme when no laser diode is used.

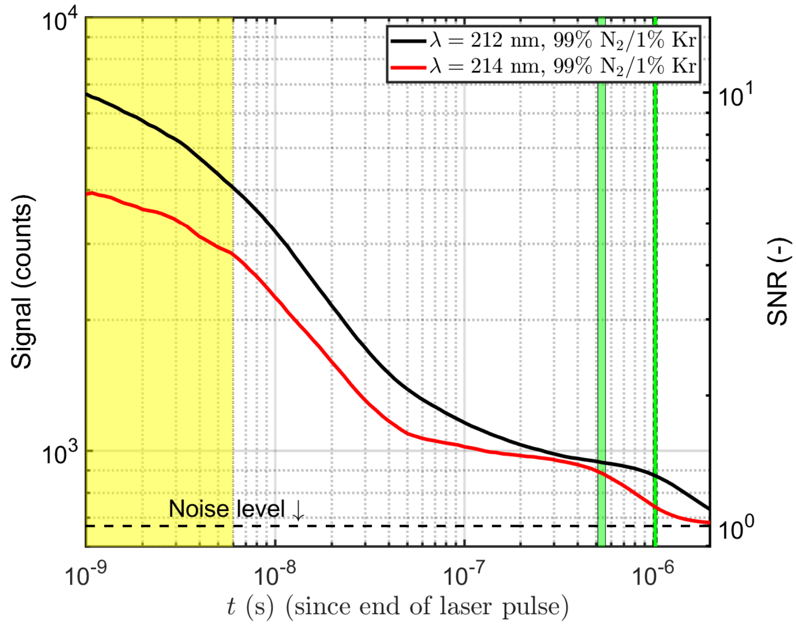

Figure 2: Time-resolved Kr Fluorescence Signal in a $P = 5$ torr, 99% N_2/1% Kr gas mixture using 212.556 nm and 214.769 nm two-photon excitation wavelengths with no read laser. The yellow region is representative of the camera gate at the write step. The two green regions are representative of the camera gate at the read step with a delay of 500 and 1000 ns respectively.

III. Relation of Cross-section to Signal-To-Noise Ratio

By definition, the fluorescence signal, Q, from an atomic transition is calculated per Eckbreth[34] as,

$$Q = hf_e N_u A \Omega V/(4\pi) \tag{1}$$

where h is Planck's constant, f_e is the frequency of emitted light, N_u is the population of the upper level, A is the overall Einstein coefficient, Ω is the collection solid angle, and V is the emitting volume. As Eq. 1 shows, SNR $\propto Q \propto N_u$.

During a laser pulse, the two-photon excited state population, denoted by N_f, is governed by

$$\frac{dN_f}{dt} = W_{f,g}N_g - (W_{pi} + A_f + W_{f,g} + q)N_f, \tag{2}$$

where $W_{f,g}$ is the two-photon excitation rate from the ground state $|g\rangle$ to final state $|f\rangle$, W_{pi} is one-photon photoionization rate from final state $|f\rangle$ to the ionized state, N_g is the population of the ground state Kr atoms, A_f is the overall Einstein coefficient, and q is the quenching rate for the excited state. At the rising edge of the laser pulse, N_f is small and is approximately proportional to $W_{f,g}$,

$$N_f \approx W_{f,g}N_g\Delta t. \tag{3}$$

The one-photon photoionization rate W_{pi} in Eq. 2 is

$$W_{pi} = F\sigma_{pi}, \tag{4}$$

where the photoionization cross-section σ_{pi} is calculated by Khambatta *et. al*[35] as

$$\sigma_{pi} = \frac{8 \times 10^{-18}}{Z_e\sqrt{\frac{-E_f}{Ry}}\left(\frac{\hbar\omega_L}{-E_f}\right)^3}. \tag{5}$$

In Eq. 5, $Z_e = 1$ is the charge of the Kr ion, Ry is the Rydberg constant, and E_f is the energy of the final state. The one-photon photoionization cross-section σ_{pi} is approximately the same for the different Kr excitation lines because of the closely clustered energies of the eight states. Therefore, the two-photon cross-section $\sigma_o^{(2)}$ is the most significant in determining the excitation spectrum for the Kr lines. Researchers, such as Saito *et al.*[30] and Khambatta *et al.*,[35] respectively developed detailed analytical and numerical population models, featuring Eq. 2. In this work, the solution to Eq. 2 is not explored beyond Eq. 3.

$W_{f,g}$ is defined as

$$W_{f,g} = F^2 \sigma^{(2)}, \tag{6}$$

where $\sigma^{(2)}$ is the two-photon excitation rate-coefficient and $F = I/(\hbar\omega_L)$ is the photon flux. I is the laser intensity; $\hbar$ is the reduced Planck's constant; and ω_L is the laser angular frequency. The rate-coefficient, $\sigma^{(2)}$, is a function of the excitation wavelength and is directly proportional to the cross-section $\sigma_o^{(2)}$. Consequently, the wavelength with the highest value of $\sigma_o^{(2)}$ will result in the highest fluorescence signal after the laser pulse. That is, SNR $\propto \sigma_o^{(2)}$ right after the rising edge of the laser pulse.

IV. Two-Photon Cross-Section Calculation for Kr for $190 - 220$ nm Excitation Range

Methods for calculating two-photon cross-sections include first-order perturbation theory, the Green's function method, R-matrix theory, and time-dependent density-functional theory (TDDFT). First-order perturbation theory for multiphoton excitation and ionization is described by Lambropoulos[36] who provides a thorough review of multiphoton processes and calculations, and demonstrates the matrix mechanics nature of the problem. Khambatta *et al.*[35,37] uses the first-order perturbation theory of Lambropoulos[36] and the oscillator formulas from Hillborn[38] to calculate two- and three-photon cross-sections for argon and krypton. He presents both a single-path and multi-path calculation. However, that calculation is limited by the availability of tabulated Einstein coefficients. Additionally in that work, the dipole-matrix element is asymmetric, thus unable to capture the mathematical symmetry of the two-photon transition matrix element. A similar single-path calculation for the excitation of Kr to the $6p$ level was made by Bokor *et al.*[39] The calculations in Bokor *et al.*[39] and Khambatta *et al.*[35,37] serve as important benchmarks for the two-photon cross-section calculation and (2+1) photoionization modeling. Mustafa *et al.*[27] used the single-path approximation to estimate the two-photon cross-section for the 212.556 nm excitation line for krypton. An additional motivation for the current work was to assess the validity of the results of Mustafa *et al.*[27] and explore if other excitation lines might result in higher fluorescence.

A two-photon cross-section calculation was conducted using multi-path, first-order accurate perturbation theory. The matrix mechanics formulation of Lambropoulos,[36] who provides a thorough review of multiphoton processes and calculations, is used because it obtains all excitation pathways for a finite basis of states. A Hartree-Fock radial wave function of the krypton ground state ($4p^6\ ^1S_0$) [a] was assumed,[40] and oscillator-strength (OS) formulas were used upon the availability of NIST transition probabilities and data.[41] We note that a Kr gas mixture with naturally-occurring isotope mole fractions was considered because the NIST line spectra database presents spectroscopic data for a naturally-occurring mixture of Kr,[41] and the laser pulse width is at least two orders of magnitude greater than the isotopic shifts of Kr. Additionally, quantum-defect theory (QDT) was used to calculate electric dipole matrix elements $\langle i | \hat{\epsilon} \cdot \vec{r} | j \rangle$ when NIST transition probabilities were unlisted. This last inclusion of QDT is key to the success of our approach as it enabled the inclusion of additional excitation pathways not included in previous works; and it determined the sign of all pathway contributions to the two-photon matrix element.

When QDT is used to evaluate the purely radial matrix elements $\langle r \rangle$, scaled hydrogen radial wave functions are constructed to represents excited Kr states. This is because a Hartree-Fock calculation showed that excited krypton states exhibited hydrogenic behavior and could be approximated well by quantum-defect radial wave functions that are calibrated by NIST line data. With the aid of QDT, a truncated spectral expansion of a Green's function was effectively constructed from a basis of intermediate Kr states ($5s$, $6s$, $7s$, $4d$, $5d$, and $6d$ states) that approximately satisfy the nonrelativistic Schrödinger equation. Within the

[a] Russell-Saunders Notation $^{2S+1}L_J$ with $S = 0$, $L = 0$, and $J = 0$.

framework of matrix mechanics, this expansion ultimately allowed the evaluation of the two-photon-transition matrix element.

The two-photon cross-section $\sigma_o^{(2)}$ is independent of laser intensity, time, and Kr concentration. It is a constant, and it is a solution to the time-independent, non-relativistic Schrödinger equation [b]. At the rising edge of the laser pulse, $\sigma_o^{(2)} \propto \sigma^{(2)} \propto Q \propto$ SNR.[34] The two-photon cross-section $\sigma_o^{(2)}$ is related to the two-photon excitation rate-coefficient $\sigma^{(2)}$ via the lineshape function $g(2\omega_L)$ as

$$\sigma^{(2)} = \sigma_o^{(2)} g(2\omega_L). \tag{7}$$

The two-photon excitation cross-section is calculated as

$$\sigma_o^{(2)} = (2\pi)^3(\alpha)^2\omega_L^2 \left| M_{fg}^{(2)} \right|^2 a_o^4, \tag{8}$$

where α is the fine structure constant, a_o is the Bohr radius, and $M_{fg}^{(2)}$ is the two-photon-transition matrix element. The line shape function $g(2\omega_L)$ is assumed to be of Gaussian form with a peak:

$$g(2\omega_L = \omega_T) = \frac{2\sqrt{\ln(2)/\pi}}{\sqrt{2(\Delta\omega_L)^2 + (\Delta\omega_T)^2}}. \tag{9}$$

The linewidth of the laser is $\Delta\omega_L$ (1350 MHz in this work), and the Doppler linewidth, $\Delta\omega_T$, is calculated by

$$\Delta\omega_T = (2\omega_L)\sqrt{\frac{8\ln(2)k_bT}{m_{kr}c^2}}, \tag{10}$$

where k_b is the Boltzmann constant, c is the speed of light, m_{kr} is the mass of one krypton atom, and T is the temperature of the Kr gas mixture.

The two-photon-transition matrix element is expressed as

$$M_{fg}^{(2)} = \sum_{k=g}^{\infty} \frac{\langle f \left| \hat{\epsilon} \cdot \vec{r} \right| k \rangle \langle k \left| \hat{\epsilon} \cdot \vec{r} \right| g \rangle}{\omega_k - \omega_g - \omega_L}. \tag{11}$$

For practical calculation on a computer, the summation over the intermediate state index k is truncated at the N^{th} state. Therefore, the transition matrix element,

$$M_{fg}^{(2)} = \sum_{k=g}^{N} \frac{\langle f \left| \hat{\epsilon} \cdot \vec{r} \right| k \rangle \langle k \left| \hat{\epsilon} \cdot \vec{r} \right| g \rangle}{\omega_k - \omega_g - \omega_L}, \tag{12}$$

is summed over a finite basis of states, such as those listed in Table 5. The truncation criterion for two-photon excitation is determined by a constraint on the maximum principal quantum number n of a bound state: n_{max}. As n becomes large, the expected radius of a one-electron atom of effective nuclear charge Z_e is $\langle r \rangle = n^2/Z_e$ in Bohr radii.[43] Per Park,[44] the $\langle r \rangle$ is proportional to the Debeye length d_D:

$$n_{\max} = \sqrt{\frac{Z_e d_D}{10a_o}} \approx \left(\frac{Z_e^2 \epsilon_o k_b}{e^2 \left(\frac{N_e}{T_e V} + \frac{N_e}{TV} \right) (10a_o)^2} \right)^{\frac{1}{4}}, \tag{13}$$

where N_e/V is the electron number density and N_i/V is the ion number density, T_e is the electron temperature, and T_i is the Kr ion temperature. The factor of $10a_o$ describes approximately the krypton van der Waals diameter and represents a 90% reduction in the Debeye potential, Φ_D, which is non-dimensionally described by $\Phi_D = 1/r \exp(-ra_o/d_D)$. For the (2+1) resonance-enhanced multiphoton excitation (REMPI) of Kr at laser wavelength $\lambda_L = 212.556$ nm, room temperature $T = 298$ K, and pressure $P = 1$ torr, the electron temperature is $T_e = 27626$ K and number densities are calculated as $N_e/V = N_i/V = 1.62 \times 10^{21}$ electrons/m^3.

[b]Relativistic effects were neglected in the Schrödinger equation because the energy of the laser was much less than the rest energy of an electron $3\hbar\omega_L \ll m_ec^2$.[42]

The electron temperature was obtained from $2(3\hbar\omega_L - |E_{ion}|)/3k_b$,[45] and number densities were obtained via the analytical population model of Saito *et al.*[30] Assuming $Z_e = 1$ for the Kr ion, the result is $n_{\max} = 7.42$. Therefore, N accommodates all states with a principal quantum number equal to or less than 7: $n \leq 7$. This is convenient because NIST transition probability data is limited for states with $n \leq 8$.[41]

An approximate Green's function, expressed as a truncated spectral expansion, is nested in the center of the expression for $M_{fg}^{(2)}$:

$$G(\vec{r}, \vec{r}\,') = \sum_{k=g}^{N} \frac{|k\rangle \langle k|}{\omega_k - \omega_g - \omega_L}. \tag{14}$$

Since Green's functions are symmetric about variable exchange ($\vec{r} \leftrightarrow \vec{r}\,'$), $G(\vec{r}, \vec{r}\,') = G(\vec{r}\,', \vec{r})$, so $M_{fg}^{(2)} = M_{gf}^{(2)}$. This mathematical property is a fundamental deviation from the oscillator-strength approach in Khambatta *et al.*,[35] which is one-sided and asymmetric. Therefore, the use of oscillator formulas, while valid, causes the loss of symmetry in the transition-matrix element. This symmetry loss is problematic in describing higher-order multiphoton excitation (three-photon and higher).

$M_{fg}^{(2)}$ is a double tensor contraction of an infinite matrix space $M = DGD$. More importantly, due to the invariance of multiphoton-excitation with respect to reference frame and basis $|k\rangle$ (See Appendix A for a proof.), $M = DGD$ is a symmetric, rank-2 tensor.

The evaluation of $M_{fg}^{(2)}$ requires the evaluation of two reduced matrix elements of the form

$$\langle i\,|\hat{\epsilon} \cdot \vec{r}|\,j\rangle = D_{ij}, \tag{15}$$

where D_{ij} is an element of the matrix representation of the dipole operator D:

$$D = \begin{bmatrix} \langle g|\hat{\epsilon}\cdot\vec{r}|g\rangle & \langle g|\hat{\epsilon}\cdot\vec{r}|1\rangle & \langle g|\hat{\epsilon}\cdot\vec{r}|2\rangle & \cdots & \cdots & \langle g|\hat{\epsilon}\cdot\vec{r}|N\rangle \\ \langle 1|\hat{\epsilon}\cdot\vec{r}|g\rangle & \langle 1|\hat{\epsilon}\cdot\vec{r}|1\rangle & \langle 1|\hat{\epsilon}\cdot\vec{r}|2\rangle & \cdots & \cdots & \langle 1|\hat{\epsilon}\cdot\vec{r}|N\rangle \\ \langle 2|\hat{\epsilon}\cdot\vec{r}|g\rangle & \langle 2|\hat{\epsilon}\cdot\vec{r}|1\rangle & \langle 2|\hat{\epsilon}\cdot\vec{r}|2\rangle & \cdots & \cdots & \langle 2|\hat{\epsilon}\cdot\vec{r}|N\rangle \\ \vdots & \vdots & \vdots & \ddots & & \vdots \\ \vdots & \vdots & \vdots & & \ddots & \vdots \\ \langle N|\hat{\epsilon}\cdot\vec{r}|g\rangle & \langle N|\hat{\epsilon}\cdot\vec{r}|1\rangle & \langle N|\hat{\epsilon}\cdot\vec{r}|2\rangle & \cdots & \cdots & \langle N|\hat{\epsilon}\cdot\vec{r}|N\rangle \end{bmatrix}. \tag{16}$$

The two indices i, j of the matrix D represent the final state $|i\rangle$ and initial state $|j\rangle$, respectively. The dipole operator, $\hat{\epsilon} \cdot \vec{r}$, describes the rotation of two electric charges of opposite sign by an external electric field. The denominator of Eq. 12,

$$G_{ii} = \frac{1}{\omega_i - \omega_g - \omega_L}, \tag{17}$$

can also be rewritten in matrix form as a diagonal matrix G:

$$G = \begin{bmatrix} \frac{1}{\omega_g - \omega_g - \omega_L} & 0 & \cdots & 0 & 0 \\ 0 & \frac{1}{\omega_1 - \omega_g - \omega_L} & \ddots & \vdots & \vdots \\ \vdots & \ddots & \ddots & \ddots & \vdots \\ \vdots & & \ddots & \frac{1}{\omega_{(N-1)} - \omega_g - \omega_L} & 0 \\ 0 & 0 & \cdots & 0 & \frac{1}{\omega_N - \omega_g - \omega_L} \end{bmatrix}. \tag{18}$$

G is the matrix representation of the Green's function, Eq. 14. Rewriting Eq. 12, the transition matrix element can be represented in matrix form:

$$M_{fg}^{(2)} = \sum_{k=g}^{N} D_{fk} G_{kk} D_{kg} = \hat{e}_f^T DGD\hat{e}_g, \tag{19}$$

where $\hat{e}_i$ is a unit vector that identifies the state of the system. For example, the vector representations of states $|g\rangle$, $|1\rangle$, $|2\rangle$, and $|N\rangle$ are

$$\hat{e}_g = \begin{Bmatrix} 1 \\ 0 \\ 0 \\ \vdots \\ 0 \end{Bmatrix}, \ \hat{e}_1 = \begin{Bmatrix} 0 \\ 1 \\ 0 \\ \vdots \\ 0 \end{Bmatrix}, \ \hat{e}_2 = \begin{Bmatrix} 0 \\ 0 \\ 1 \\ \vdots \\ 0 \end{Bmatrix}, \text{ and } \hat{e}_N = \begin{Bmatrix} 0 \\ 0 \\ 0 \\ \vdots \\ 1 \end{Bmatrix}. \tag{20}$$

Eq. 19 substantiates to a rank 2 tensor contraction of the Green's function matrix G. The f^{th} row of matrix D is post-multiplied by the matrix G, which is then post-multiplied by the g^{th} column of matrix D, resulting in the scalar $M_{fg}^{(2)}$.

IV.A. The Calculation of Dipole Matrix Elements D_{ij} Using QDT

In this section, the dipole matrix elements D_{ij} are calculated via the central-field approximation,[43,46] which allows one to separate the effects of angular and radial components in the Schrödinger equation, expressed in spherical coordinates. This allows a state $|k\rangle$ to be expressed as a product of one-electron, radial wave functions $R_{nl}(r) \cdot \prod_p R_p(r_p)$ multiplied by a tensor spherical harmonic $\mathbf{Y}_{JM}^{LS}(\theta, \phi)$. Here, subscript p denotes an unexcited krypton electron, and nl denotes the quantum numbers of the valence electron to be excited by the laser. This state is represented as $|\mathbf{n}LSJM\rangle$, assuming LS spin-orbit coupling. The radius of the excited valence electron from the Kr nucleus is r. The orientation of its angular momentum is described by azimuth angle θ and polar angle ϕ. The set of all principal quantum numbers for the Kr atom is $\mathbf{n}$, and the principal quantum number of the excited electron is n. L is the total orbital angular momentum quantum number of the atom, and l is the single-electron angular momentum number of the excited electron. S is the total electron spin quantum number of the atom. For a true dipole moment transition, S remains constant because the dipole moment operator $\hat{\epsilon} \cdot \vec{r}$ does not act on electron spin coordinates. The dipole moment operator is solely written in terms of scalar spherical harmonics:[46]

$$\hat{\epsilon} \cdot \vec{r} = \sqrt{\frac{4\pi}{3}} r \sum_{q=(0,\pm 1)} \epsilon_q Y_1^q, \tag{21}$$

where the polarization component is ϵ_q; $q = 0$ for linear polarization; $q = 1$ for right-handed circular polarization; and $q = -1$ for left-handed polarization of the laser's electric field.[47] The orientation of the laser electric field defines the orientation of the z-axis in the spherical coordinate system imposed on the nucleus of a Kr atom.

To evaluate the reduced matrix elements D_{ij}, a simplified expression must first be obtained. By applying the Wigner-Eckart Theorem,[47] D_{ij} may be rewritten as

$$\begin{aligned} D_{ij} &= \langle i \,|\hat{\epsilon} \cdot \vec{r}|\, j\rangle \\ &= \langle \mathbf{n}_i L_i S_i J_i M_i \,|\hat{\epsilon} \cdot \vec{r}|\, \mathbf{n}_j L_j S_j J_j M_j\rangle \\ &= \langle \mathbf{n}_i L_i S_i J_i \,|\vec{r}|\, \mathbf{n}_j L_j S_j J_j\rangle \\ &\quad \times \sum_{q=(0,\pm 1)} \epsilon_q \begin{pmatrix} J_i & 1 & J_j \\ -M_i & q & M_j \end{pmatrix} (-1)^{1-J_j-M_i}. \end{aligned} \tag{22}$$

By using the definition of a vector $\vec{r} = r\hat{e}_r$, radial coordinates are separated from angular coordinates:

$$\begin{aligned} D_{ij} &= \langle i \,|r|\, j\rangle \langle L_i S_i J_i \,|\hat{e}_r|\, L_j S_j J_j\rangle \\ &\quad \times \sum_{q=(0,\pm 1)} \epsilon_q \begin{pmatrix} J_i & 1 & J_j \\ -M_i & q & M_j \end{pmatrix} (-1)^{1-J_j-M_i}. \end{aligned} \tag{23}$$

Using the following expression from Messiah[47] (Eq. C.89) for reduced matrix elements and irreducible tensor operators of tensor rank k,

$$\begin{aligned}
&\left\langle \tau_1\tau_2 J_1 J_2 J \left| T^{(k)} \right| \tau_1'\tau_2' J_1' J_2' J' \right\rangle = \\
&\quad \delta_{\tau_2\tau_2'}\delta_{J_2 J_2'} \left\langle \tau_1 J_1 \left| T^{(k)} \right| \tau_1' J_1' \right\rangle (-1)^{J'+J_1+J_2+k} \\
&\qquad \times \sqrt{(2J+1)(2J'+1)} \left\{ \begin{array}{ccc} J_1 & k & J_1' \\ J' & J_2 & J \end{array} \right\},
\end{aligned} \tag{24}$$

the angular term $\langle L_i S_i J_i \left| \hat{e}_r \right| L_j S_j J_j \rangle$ can be further simplified, noting $\tau_1 = \tau_1' = \tau_2 = \tau_2' = 1$. The reduced matrix element D_{ij} becomes

$$\begin{aligned}
D_{ij} = {} & \delta_{S_i S_j} \langle r \rangle \langle L_i \left| \hat{e}_r \right| L_j \rangle (-1)^{L_i+J_j+S_i+1} \\
& \times \sqrt{(2J_i+1)(2J_j+1)} \left\{ \begin{array}{ccc} L_i & 1 & L_j \\ J_j & S_j & J_i \end{array} \right\} \\
& \times \sum_{q=(0,\pm 1)} \epsilon_q \left(\begin{array}{ccc} J_i & 1 & J_j \\ -M_i & q & M_j \end{array} \right) (-1)^{1-J_j-M_i},
\end{aligned} \tag{25}$$

where $\langle r \rangle = \langle i \left| r \right| j \rangle$ is the purely radial matrix element. The term $\delta_{S_i S_j}$ implies that the dipole moment operator does not act on electron coordinates. Next, using the Wigner-Eckart Theorem[47] for the expected value of a spherical tensor Y_k of rank k,

$$\begin{aligned}
&\langle l_1 \left| Y_k \right| l_2 \rangle = \\
&\quad = (-1)^{l_1} \sqrt{\frac{(2l_1+1)(2k+1)(2l_2+1)}{4\pi}} \left(\begin{array}{ccc} l_1 & k & l_2 \\ 0 & 0 & 0 \end{array} \right)
\end{aligned} \tag{26}$$

the expected value of the rank-1 unit vector $\hat{e}_r$, $\langle L_i \left| \hat{e}_r \right| L_j \rangle$, can be evaluated. D_{ij} becomes

$$\begin{aligned}
D_{ij} = {} & \delta_{S_i S_j} \langle r \rangle \sqrt{(2L_i+1)(2L_j+1)} \\
& \times \left(\begin{array}{ccc} L_i & 1 & L_g \\ 0 & 0 & 0 \end{array} \right) \sqrt{(2J_i+1)(2J_j+1)} \\
& \times (-1)^{2L_i+J_j+S_i+1} \left\{ \begin{array}{ccc} L_i & 1 & L_j \\ J_j & S_j & J_i \end{array} \right\} \\
& \times \sum_{q=(0,\pm 1)} \epsilon_q \left(\begin{array}{ccc} J_i & 1 & J_j \\ -M_i & q & M_j \end{array} \right) (-1)^{1-J_j-M_i},
\end{aligned} \tag{27}$$

which rearranges into

$$\begin{aligned}
D_{ij} = {} & \delta_{S_i S_j} \langle r \rangle \sqrt{(2J_i+1)(2J_j+1)(2L_i+1)(2L_j+1)} \\
& \times \left(\begin{array}{ccc} L_i & 1 & L_g \\ 0 & 0 & 0 \end{array} \right) \left\{ \begin{array}{ccc} L_i & 1 & L_j \\ J_j & S_j & J_i \end{array} \right\} (-1)^{2L_i+J_j+S_i+1} \\
& \times \sum_{q=(0,\pm 1)} \epsilon_q \left(\begin{array}{ccc} J_i & 1 & J_j \\ -M_i & q & M_j \end{array} \right) (-1)^{1-J_j-M_i}.
\end{aligned} \tag{28}$$

For allowable dipole transitions, the effect of the factor of $-1^{-J_j-M_i+1}$, which arises from the definition of the Wigner-Eckart Theorem, has no effect on the transition matrix element summation due to the consistent parity of J, as shown in Table 3.

Table 3: Parity Table for term $-1^{-J_j-M_i+1}$. $J_j = 0, 1$ correspond to 2-photon transitions, and $J_j = 0, 1, 2$ correspond to 3-photon transitions. The term $-1^{-J_j-M_i+1}$ does not contribute to the transition matrix element summation because it is consistently the same value for each stage of a multiphoton transition for all possible pathways.

J_j	0		1		2	
M_i	0	1	0	-2	0	3
$-1^{-J_j-M_i+1}$	-1	1	1	1	-1	1

The 2×3 matrix terms in parentheses are $3j$-Wigner Symbols, and the 2×3 matrix term in brackets is the $6j$-Wigner Symbol. $3j$-Wigner Symbols enforce dipole moment selection rules, and the $6j$-Wigner Symbol quantifies the degeneracy of a transition occurring (it amounts to a normalization factor). Our research only considers linear polarization of the laser electric field, $q = 0$, forcing $M_i = M_j = 0$ for all transitions $j \to i$. $S_i = S_j = 0$ for all transitions because the Kr ground state has a total electron spin of zero, and the dipole moment operator $\hat{\epsilon}\cdot\vec{r}$ does not act on electron spin coordinates. L_i is the norm of the addition of two angular momenta, $L_i = |\vec{l_i} + \vec{l_g}|$, which describes the angular momentum coupling between the excited electron and a $4p$ valence electron of opposite electron spin. Since the dipole moment operator does not operate on electron coordinates, it turns out that $L_i = J_i$ for the dipole transitions we analyzed. A cartoon summarizing how angular momentum changes during $(2+1)$-photoionization is shown in Fig. 3, and an angular momentum table is provided in Table 4 to show how to calculate the coupled quantum L from the angular momenta of two electrons, each with an azimuth orbital quantum number $m = 0$.

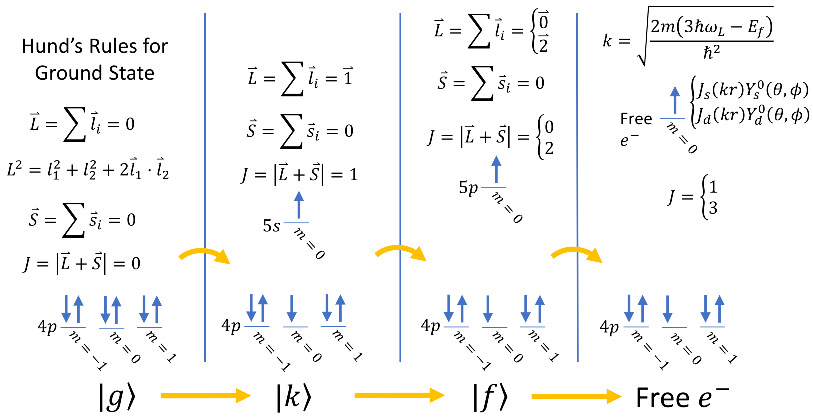

Figure 3: Angular momenta of a Kr atom during linearly polarized $(2+1)$ multiphoton photoionization. This cartoon demonstrates LS spin-orbit coupling for each Kr state at each stage of excitation: ground state $|g\rangle$, intermediate state $|k\rangle$, two-photon state $|f\rangle$, and ionized state e^-. For dipole transitions, $\Delta S = 0$ and consequently, $J = L$.

Table 4: Addition of the angular momentum of two electrons l_1 and l_2: $\vec{L} = \vec{l_1} + \vec{l_2}$. $m = 0$ for both electrons.

State	$L^2 = l_1^2 + l_2^2 + 2\vec{l_1}\cdot\vec{l_2}$	L	J
$\lvert g\rangle$	$1^2 + 1^2 + 2(1)(-1) = 0$	0	0
$\lvert k\rangle$	$1^2 + 0^2 + 2(1)(0) = 1$	1	1
$\lvert f\rangle$	$1^2 + 1^2 + 2(1)(\pm 1) = \begin{Bmatrix} 4 \\ 0 \end{Bmatrix}$	$\begin{Bmatrix} 2 \\ 0 \end{Bmatrix}$	$\begin{Bmatrix} 2 \\ 0 \end{Bmatrix}$

Therefore, the simplified dipole matrix element is

$$\begin{aligned} D_{ij} &= \delta_{l_i,l_j\pm 1} \langle r \rangle (2J_i+1)(2J_j+1) \\ &\times \begin{pmatrix} J_i & 1 & J_j \\ 0 & 0 & 0 \end{pmatrix}^2 \begin{Bmatrix} J_i & 1 & J_j \\ J_j & 0 & J_i \end{Bmatrix}, \end{aligned} \tag{29}$$

noting that for a dipole transition $\Delta l = \pm 1$. The factor of $(-1)^{2L_i+J_j+S_i+1}$ is omitted because it does not contribute any meaningful sign change in the summation. For dipole moments, parity is conserved, resulting in consistent state parity. $S_i + 1$ is always 1; $2L_i$ is always even; and -1^{J_j} is consistent for all considered transitions. More interestingly, due to the consistent parity of J for transition states, Eq. 29 is symmetric about variable exchange $i \leftrightarrow j$, which conforms to the symmetry property of a Green's function Eq. 14. Using identity (C.37) from,[47] Eq. 29 can be further simplified to

$$\begin{aligned} D_{ij} &= \delta_{l_i,l_j\pm 1} \langle r \rangle \sqrt{(2J_i+1)(2J_j+1)} \\ &\times \begin{pmatrix} J_i & 1 & J_j \\ 0 & 0 & 0 \end{pmatrix}^2 . \end{aligned} \tag{30}$$

Now, the main difficulty with calculating D_{ij} is the evaluation of the radial wave function integral $\langle r \rangle$:

$$\begin{aligned} \langle r \rangle &= \langle R_i(r) \, |r| \, R_j(r) \rangle \prod_p \langle R_{i,p}(r_p) | R_{j,p}(r_p) \rangle \\ &= \int_0^\infty r^3 R_i(r) R_j(r) dr \end{aligned} \tag{31}$$

because the form of the wave functions $R_i(r)$ must be assumed from prior knowledge. The one-electron model of Kr also assumes that only the radial wave function of the excited electron changes, an assumption justified by a Hartree-Fock calculation.[40] Therefore, $\prod_p \langle R_{i,p}(r_p)|R_{j,p}(r_p)\rangle = 1$ due to the normalization of the radial wave functions.

Excited states of noble gas atoms approximate one-electron atoms, and to first order, electric dipoles. Quantum-defect theory correctly assumes that the excited states of atoms exhibit scaled, hydrogen-like behavior, as verified by our Hartree-Fock calculation shown in Fig. 4. This observation was first made by Rydberg[48] and was later exploited by Bethe *et al.*,[42] Bebb *et al.*,[49] and McGuire.[50,51] While Hartree-Fock iterates for an explicit electron repulsion potential,[40,46] quantum-defect theory directly incorporates the effect of electron repulsion through the use of excited state energy as an input to scale the wave function. With the verified assumption of hydrogenic behavior for excited Kr states, quantum-defect radial wave functions can be used with confidence to describe the excited states of Kr.

Properly normalized hydrogen radial wave functions[52] are expressed as

$$\begin{aligned} R_{nl}(r) = & \sqrt{\left[\frac{(n-l-1)!}{2n((n+l)!)} \left(\frac{2Z_e}{n} \right)^3 \right]} \left(\frac{2Z_e r}{n} \right)^l \\ & \times \exp\left(\frac{-Z_e r}{n} \right) L_{n-l-1}^{2l+1} \left(\frac{2Z_e r}{n} \right), \end{aligned} \tag{32}$$

with effective nuclear charge $Z_e = 1$ and energy $E_n = -Ry/n^2$. Meanwhile, quantum-defect radial wave functions[48] are scaled hydrogen radial wave functions and are written similarly as

$$\begin{aligned} R_{nl}(E, I_m, r) = & \frac{2}{(n^*)^2} \sqrt{\frac{\Gamma(n-l-I_m(l))}{\Gamma(n^*+l^*+1)}} \left(\frac{2r}{n^*} \right)^l \\ & \times \exp\left(\frac{-r}{n^*} \right) L_{n-l-I_m(l)-1}^{2l^*+1} \left(\frac{2r}{n^*} \right), \end{aligned} \tag{33}$$

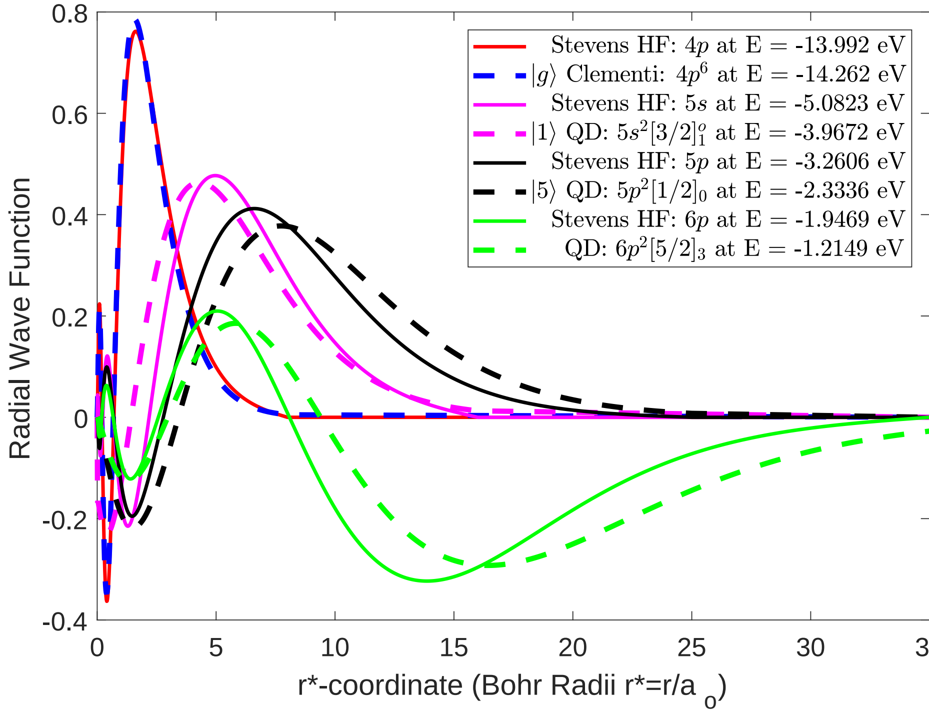

Figure 4: Comparison between Hartree-Fock (HF) Radial Orbitals and Quantum Defect (QD) Radial Orbitals. This plot demonstrates the hydrogen-like behavior of Kr radial wave functions. This plot justifies the use of quantum defect orbitals and validates Rydberg's original observation of the hydrogenic behavior of atoms.[48]

where the effective principal quantum number is

$$n^* = n - \delta_d, \tag{34}$$

the quantum defect is

$$\delta_d = n - \sqrt{\frac{-Ry}{E}}, \tag{35}$$

and the effective angular momentum quantum number is

$$l^* = l - \delta_d + I_m(l). \tag{36}$$

Γ is the gamma function; ( )! is the factorial function; and $L_n^y(x)$ is the associated Laguerre polynomial function of degree n and input y evaluated at x. Eq. 33 is a scaled version of Eq. 32.

Quantum-defect radial wave functions are generated by four input parameters n, l, E, and I_m, which are determined by NIST data[41] and are listed in Table 5 for a basis of Kr states. n and l are reported in the Racah notation of a state. Absolute energy E is obtained by subtracting the first ionization energy of Kr (13.9996053 eV) from the reported NIST energy because NIST reports energy relative to the ground state. For the selection of the integer I_m, Einstein coefficients are used to ensure that the radial wave functions reflect experimental observations. Also, $(\delta_d - l - 1/2) \leq I_m < (n - l - 1)$.[48] By minimizing the discrepancy between calculated Einstein coefficients,[38]

$$A_{ij} = \frac{2e^2\omega_{ij}^3 a_o^2}{3c^3 h\epsilon_o} \sum_{m_j} \left| \langle n_i l_i m_i | \vec{r} | n_j l_j m_j \rangle \right|^2, \tag{37}$$

and tabulated NIST Einstein coefficients through integer variation of I_m, acceptable radial wave functions are constructed for excited Kr states.

Table 5: Input Parameters for Quantum-Defect Radial Wave Functions. This table also provides the basis of states used to calculate two-photon transition matrix element. Data was obtained from NIST.[41] States $|5\rangle$, $|6\rangle$, $|9\rangle$, $|11\rangle$, $|12\rangle$, $|15\rangle$, $|16\rangle$, and $|17\rangle$ are of critical interest for the laser excitation lines considered in this paper. The two-photon excitation wavelengths, λ_L, are measured in vacuum.

Index	State (Term Symbol)[c]	n	l	E (eV)	I_m	λ_L (nm)
g	$4p^6\ ^1S_0$	4	1	-13.9996053	-	-
1	$(^2P^o_{3/2})5s\ ^2[3/2]^o_1$	5	0	-3.96720476	3	-
2	$(^2P^o_{3/2})5s\ ^2[3/2]^o_2$	5	0	-4.08437309	2	-
3	$(^2P^o_{1/2})5s\ ^2[1/2]^o_1$	5	0	-3.35597053	3	-
4	$(^2P^o_{1/2})5s\ ^2[1/2]^o_0$	5	0	-3.43719109	2	-
5	$(^2P^o_{3/2})5p\ ^2[1/2]_0$	5	1	-2.33357724	3	212.556
6	$(^2P^o_{3/2})5p\ ^2[3/2]_2$	5	1	-2.45378261	1	214.769
7	$(^2P^o_{3/2})5p\ ^2[1/2]_1$	5	1	-2.69615013	2	219.374
8	$(^2P^o_{3/2})5p\ ^2[5/2]_3$	5	1	-2.55655804	3	216.698
9	$(^2P^o_{3/2})5p\ ^2[5/2]_2$	5	1	-2.55494904	1	216.667
10	$(^2P^o_{3/2})5p\ ^2[3/2]_1$	5	1	-2.47348948	1	215.136
11	$(^2P^o_{1/2})5p\ ^2[3/2]_2$	5	1	-1.85595245	2	204.196
12	$(^2P^o_{1/2})5p\ ^2[1/2]_0$	5	1	-1.74313881	2	202.316
13	$(^2P^o_{1/2})5p\ ^2[1/2]_1$	5	1	-1.85917847	1	204.250
14	$(^2P^o_{1/2})5p\ ^2[3/2]_1$	5	1	-1.89925407	1	204.927
15	$(^2P^o_{3/2})6p\ ^2[1/2]_0$	6	1	-1.13480243	3	192.749
16	$(^2P^o_{3/2})6p\ ^2[3/2]_2$	6	1	-1.18427475	3	193.494
17	$(^2P^o_{3/2})6p\ ^2[5/2]_2$	6	1	-1.21421328	2	193.947
18	$(^2P^o_{1/2})6s\ ^2[1/2]_1$	6	0	-0.963121959	2	-
19	$(^2P^o_{3/2})6s\ ^2[3/2]_1$	6	0	-1.614321866	1	-
20	$(^2P^o_{1/2})7s\ ^2[1/2]_1$	7	0	-0.885709772	1	-
21	$(^2P^o_{3/2})4d\ ^2[3/2]_1$	4	2	-1.645049675	1	-
22	$(^2P^o_{3/2})5d\ ^2[1/2]_1$	5	2	-1.129823313	2	-
23	$(^2P^o_{3/2})6d\ ^2[3/2]_1$	6	2	-0.577230406	1	-
24	$(^2P^o_{3/2})6d\ ^2[1/2]_1$	6	2	-0.649464393	3	-

The initial state $|i\rangle$ has a degenerate azimuth quantum number m_i. In a pure dipole moment transition, the only active quantum number is the angular momentum quantum number l. Unlike Hillborn,[38] a weighted summation must take place over both m_i and m_j to account for the degeneracy of both quantum numbers in an isotropic electric field $q = 0, \pm 1$. Therefore,

$$\begin{aligned}
A_{ij} &= \frac{2e^2\omega_{ij}^3 a_o^2}{3c^3 h\epsilon_o} \sum_{m_i} \frac{1}{\sqrt{w_t}} \sum_{m_j} \sum_{q=0,\pm1} |\langle n_i l_i m_i | \vec{r} | n_j l_j m_j \rangle|^2 \\
. &= \frac{2e^2\omega_{ij}^3 a_o^2}{3c^3 h\epsilon_o} \left[\langle r \rangle \sqrt{\frac{(2l_i+1)(2l_j+1)}{w_t}} \begin{pmatrix} l_i & 1 & l_j \\ 0 & 0 & 0 \end{pmatrix} \right]^2 \\
&= \frac{2e^2\omega_{ij}^3 a_o^2}{3c^3 h\epsilon_o} \left[\langle r \rangle \frac{1}{\sqrt{3}} \right]^2 \quad \text{for s} \Leftrightarrow \text{p transitions} \\
&= \frac{2e^2\omega_{ij}^3 a_o^2}{3c^3 h\epsilon_o} \left[\langle r \rangle \sqrt{\frac{2}{9}} \right]^2 \quad \text{for p} \Leftrightarrow \text{d transitions,}
\end{aligned} \tag{38}$$

where w_t is the number of nonzero transitions produced by the degeneracy of m_i and m_j in an isotropic radiation field. $1/w_t$ is the probability of a transition occurring. See Appendix B for the determination of w_t. For fixed l_i and l_j, the value of w_t can be determined from the number of nonzero Clebsch-Gordon coefficients for varying m_i, m_j, and polarization component q. For $s \leftrightarrow p$ transitions, $w_t = 3$; and for $p \leftrightarrow d$ transitions, $w_t = 9$. Eq. 38 amounts to practical means to calculate Einstein coefficients from a set of radial wave functions. Results are shown in Table 6. For the ground state $|g\rangle$, a Hartree-Fock radial orbital, composed of a linear combination of Slater-type orbitals, from Clementi *et al.*[40] is used:

$$
\begin{aligned}
R_{4p}(r) = \quad & 0.08488 \times \mathrm{STO}(2, 17.03660, r) + \\
& 0.00571 \times \mathrm{STO}(2, 26.04380, r) + \\
& 0.04169 \times \mathrm{STO}(3, 15.51000, r) + \\
& -0.07425 \times \mathrm{STO}(3, 9.49403, r) + \\
& -0.26866 \times \mathrm{STO}(3, 6.57275, r) + \\
& 0.01341 \times \mathrm{STO}(4, 5.38507, r) + \\
& 0.51241 \times \mathrm{STO}(4, 3.15603, r) + \\
& 0.42557 \times \mathrm{STO}(4, 2.02966, r) + \\
& 0.18141 \times \mathrm{STO}(4, 1.42733, r),
\end{aligned}
\tag{39}
$$

where the normalized Slater Type Orbital (STO) function is defined as

$$
\mathrm{STO}(n, \zeta, r) = \frac{1}{\sqrt{(2n)!}} (2\zeta)^{(n+1/2)} r^{n-1} e^{-\zeta r}. \tag{40}
$$

This ground-state Hartree-Fock radial wave function assumes a spherically symmetric electric charge distribution and accounts to first order the electron-repulsion exerted on a $4p$ electron. Electron repulsion shields a valence $4p$ electron from the attractive potential of the Kr nucleus, increasing its ground state energy beyond that of a pure one-electron atom of atomic number $Z = 36$. In eq. (40), ζ is interpreted as a shielding parameter obtained by curve fitting the numerical results of a Hartree-Fock calculation.

In Table 6, Einstein coefficients are calculated via Eq. 38 with varying accuracy but to the correct order of magnitude. The QDT parameter, I_m, is tuned to maximize the accuracy of A_{ij}. By obtaining the correct order of magnitude and in some cases the correct Einstein coefficient, Table 6 further validates the use of quantum-defect radial wave functions Eq. 33.

With a basis of wave functions calibrated on NIST atomic spectra data, Eqs. 19 and 8 are directly evaluated, producing the two-photon cross-section data shown in Fig. 5. The values of cross-sections are shown in Tables 7, 8, and 9. When quantum-defect radial wave functions are used in conjunction with oscillator strength formulas for linear polarization,[37] such as

$$
\langle i| \hat{\epsilon} \cdot \vec{r} |j\rangle = \sqrt{\frac{3A_{ij}hc^3\epsilon_o}{2e^2\omega_{ij}}} \sqrt{2J_i + 1} \begin{pmatrix} J_i & 1 & J_j \\ 0 & 0 & 0 \end{pmatrix}, \tag{41}
$$

good agreement is obtained with the Richardson *et al.*[13] excitation spectrum, especially using basis sets 2 and 3, which include d orbitals. In Table 10, single-path cross-section results are also calculated and tabulated for comparison to results listed in Table 9.

The resulting approach is a hybrid method for the evaluation of dipole matrix elements, consisting of quantum defect theory and where possible, oscillator strengths. Another contribution of quantum defect theory is the prediction of the sign of the radial matrix element from the evaluation of Eq. 31. The oscillator strength, Eq. 41, must retain the same sign as Eq. 31 and Eq. 29. This sign determines which excitation pathways make constructive and destructive contributions to the two-photon transition matrix element. Also, wherever Eq. 41 is used for the evaluation of a matrix element, the equality, $D_{ij} = D_{ji}$, must be

[c]Two Notations:[41] (1) Russell-Saunders ${}^{2S+1}L_J$ notation for Kr ground state $|g\rangle$. (2) Racah $({}^{2S_1+1}P^o_{J_1})\ nl^{(2S_1+1)}[K]_J{}^o$ notation[d] for excited Kr states. $\vec{K} = \vec{J_1} + \vec{l}$; $\vec{J} = \vec{K} + \vec{s}$; and $\vec{K} = \vec{L} + \vec{S_1}$.[41] S_1 is the total electron spin of the ion, s is the spin of the excited electron, and L is the total orbital angular momentum. $\vec{S} = \vec{S_1} + \vec{s}$.

Table 6: Calculation of Einstein coefficients using quantum defect functions and comparison with NIST experimental data.[41]

NIST				Quantum Defect Theory	
Transition	Wavelength (nm)	$A_{ij}(1/s)$	Acc.[e]	A_{ij} (1/s)	% Error
$\|23\rangle \to \|g\rangle$	92.3713	1.14×10^8	C	4.16×10^7	63.5%
$\|24\rangle \to \|g\rangle$	92.8711	3.87×10^6	C	2.64×10^5	93.2%
$\|22\rangle \to \|g\rangle$	96.3374	3.35×10^7	C	2.13×10^7	36.3%
$\|20\rangle \to \|g\rangle$	94.5441	2.81×10^8	C	1.0450×10^8	62.8%
$\|18\rangle \to \|g\rangle$	95.1056	2.58×10^7	C	6.8928×10^7	167.2%
$\|19\rangle \to \|g\rangle$	100.1061	3.42×10^8	C	2.68×10^8	21.5%
$\|21\rangle \to \|g\rangle$	100.3550	1.82×10^8	C	1.37×10^8	24.8%
$\|3\rangle \to \|g\rangle$	116.4867	3.09×10^8	$A+$	2.33×10^8	24.5%
$\|1\rangle \to \|g\rangle$	123.5838	2.98×10^8	$A+$	4.97×10^8	66.7%
$\|15\rangle \to \|2\rangle$	427.5172	1.99×10^6	$C+$	1.74×10^6	12.7%
$\|16\rangle \to \|1\rangle$	437.7351	3.74×10^6	B	2.45×10^6	34.4%
$\|15\rangle \to \|1\rangle$	445.5168	3.97×10^5	B	4.92×10^5	23.9%
$\|17\rangle \to \|1\rangle$	450.3617	7.8×10^5	C	4.59×10^6	488.7%
$\|5\rangle \to \|1\rangle$	758.7414	4.310×10^7	$A+$	4.77×10^7	10.8%
$\|6\rangle \to \|2\rangle$	760.1546	2.732×10^7	AA	2.78×10^7	1.8%
$\|12\rangle \to \|3\rangle$	768.7361	4.064×10^7	AA	2.98×10^7	26.8%
$\|10\rangle \to \|2\rangle$	769.6658	4.27×10^6	A	2.74×10^7	540.9%
$\|13\rangle \to \|4\rangle$	785.6984	2.041×10^7	A	2.14×10^7	5.0%
$\|14\rangle \to \|4\rangle$	806.1721	1.583×10^7	$B+$	2.19×10^7	38.6%
$\|8\rangle \to \|2\rangle$	811.5132	3.610×10^7	AAA	3.50×10^7	3.10%
$\|6\rangle \to \|1\rangle$	819.2308	8.94×10^6	A	2.75×10^7	207.3%
$\|11\rangle \to \|3\rangle$	826.5514	3.416×10^7	AA	2.93×10^7	14.2%
$\|9\rangle \to \|1\rangle$	877.9161	2.217×10^7	AA	2.43×10^7	9.66%
$\|7\rangle \to \|3\rangle$	893.1145	2.289×10^7	A	2.24×10^7	2.02%

used to ensure symmetry. This properly interfaces quantum-defect theory with oscillator strength formulas, creating the hydrid dipole matrix element evaluation method and thus allowing for the eventual extension of Eq. 19 to general multiphoton excitation. For example, for three photon excitation, the entire dipole matrix D is used:

$$M_{fg}^{(3)} = \sum_{k=g}^{N} \sum_{p=g}^{N} D_{fk} G_{kk} D_{kp} G_{pp} D_{pg} = \hat{e}_f^T D G D G D \hat{e}_g. \tag{42}$$

When using a hybrid dipole matrix element calculation scheme, selection of states with adequate experimental data is crucial for reasonable results. Insufficient transition probability data rendered some state omissions in the finite basis of states listed in Table 5. For example, only one $4d$ orbital, state $|21\rangle$, was used in basis sets 2 and 3 (Tables 8 and 9) because it had the highest, observed transition probability of all $4d$ states between itself and ground, and it had the highest experimentally measured, transition probability between itself and a $5p$ state: $|21\rangle \to |10\rangle$. It was the only state with high transition probabilities between $4d$ and $5p$ levels. More importantly, state $|21\rangle$ exhibited dipole-moment behavior, which could be described by quantum-defect theory. The effect of other $4d$ orbitals on the excitation process is small but can be better determined once more transition probabilities become available for transitions between $4d$ and $5p$ states. However, the inclusion of other $4d$ states will not significantly change the excitation spectrum shown in Fig. 5. The same reasoning was made for the inclusion of $5d$ and $6d$ states in basis set 3.

Table 7: Two-photon Cross-sections using Basis Set 1: $5s$, $6s$, and $7s$ states.

Basis	Basis Set 1: $\vert g\rangle, \vert 1\rangle, \vert 2\rangle, \ldots \vert 17\rangle$					
Theory	Quantum-Defect			Quantum-Defect with Oscillator Strengths		
λ_L (nm)	$\sigma_o^{(2)}$ (cm^4)	$\sigma^{(2)} = \sigma_o^{(2)} g(2\omega_L)$ $(cm^4 \cdot s)$	$\frac{\sigma^{(2)}}{\vert\vert\sigma^{(2)}\vert\vert_\infty}$	$\sigma_o^{(2)}$ (cm^4)	$\sigma^{(2)} = \sigma_o^{(2)} g(2\omega_L)$ $(cm^4 \cdot s)$	$\frac{\sigma^{(2)}}{\vert\vert\sigma^{(2)}\vert\vert_\infty}$
192.749	7.02×10^{-37}	2.29×10^{-47}	0.005	1.73×10^{-36}	5.65×10^{-47}	0.016
193.494	5.01×10^{-37}	1.64×10^{-47}	0.003	3.70×10^{-38}	1.21×10^{-48}	0.0003
193.947	7.28×10^{-37}	2.39×10^{-47}	0.005	1.25×10^{-37}	4.10×10^{-48}	0.001
202.316	2.17×10^{-35}	7.39×10^{-46}	0.151	6.67×10^{-37}	2.27×10^{-47}	0.006
204.196	2.55×10^{-35}	8.74×10^{-46}	0.178	3.84×10^{-37}	1.32×10^{-47}	0.004
212.556	1.39×10^{-34}	4.91×10^{-45}	1.000	1.03×10^{-34}	3.63×10^{-45}	1.000
214.769	5.56×10^{-35}	1.98×10^{-46}	0.404	3.30×10^{-35}	1.18×10^{-45}	0.324
216.667	6.23×10^{-35}	2.24×10^{-46}	0.455	3.92×10^{-35}	1.41×10^{-45}	0.388

Table 8: Two-photon Cross-sections using only Basis Set 2: $5s$, $6s$, $7s$, and $4d$ states.

Basis	Basis Set 2: $\vert g\rangle, \vert 1\rangle, \vert 2\rangle, \ldots \vert 18\rangle$					
Theory	Quantum-Defect			Quantum-Defect with Oscillator Strengths		
λ_L (nm)	$\sigma_o^{(2)}$ (cm^4)	$\sigma^{(2)} = \sigma_o^{(2)} g(2\omega_L)$ $(cm^4 \cdot s)$	$\frac{\sigma^{(2)}}{\vert\vert\sigma^{(2)}\vert\vert_\infty}$	$\sigma_o^{(2)}$ (cm^4)	$\sigma^{(2)} = \sigma_o^{(2)} g(2\omega_L)$ $(cm^4 \cdot s)$	$\frac{\sigma^{(2)}}{\vert\vert\sigma^{(2)}\vert\vert_\infty}$
192.749	2.56×10^{-35}	8.37×10^{-46}	0.094	2.80×10^{-35}	9.15×10^{-46}	0.133
193.494	9.85×10^{-35}	7.42×10^{-46}	0.084	1.60×10^{-35}	5.26×10^{-46}	0.077
193.947	1.73×10^{-35}	5.67×10^{-46}	0.064	1.20×10^{-35}	3.93×10^{-46}	0.057
202.316	1.04×10^{-34}	3.55×10^{-45}	0.400	1.95×10^{-35}	6.61×10^{-46}	0.0963
204.196	9.85×10^{-35}	3.37×10^{-45}	0.381	1.57×10^{-35}	5.39×10^{-46}	0.0784
212.556	2.51×10^{-34}	8.86×10^{-45}	1.000	1.94×10^{-34}	6.87×10^{-45}	1.000
214.769	1.32×10^{-34}	4.71×10^{-45}	0.531	3.95×10^{-35}	1.41×10^{-45}	0.205
216.667	1.38×10^{-34}	4.95×10^{-45}	0.559	6.34×10^{-35}	2.28×10^{-45}	0.331

Table 9: Two-photon Cross-sections using only Basis Set 3: $5s$, $6s$, $7s$, $4d$, $5d$, and $6d$ states.

Basis	Basis Set 3: $\vert g\rangle, \vert 1\rangle, \vert 2\rangle, \ldots \vert 21\rangle$					
Theory	Quantum-Defect			Quantum-Defect with Oscillator Strengths		
λ_L (nm)	$\sigma_o^{(2)}$ (cm^4)	$\sigma^{(2)} = \sigma_o^{(2)} g(2\omega_L)$ $(cm^4 \cdot s)$	$\frac{\sigma^{(2)}}{\vert\vert\sigma^{(2)}\vert\vert_\infty}$	$\sigma_o^{(2)}$ (cm^4)	$\sigma^{(2)} = \sigma_o^{(2)} g(2\omega_L)$ $(cm^4 \cdot s)$	$\frac{\sigma^{(2)}}{\vert\vert\sigma^{(2)}\vert\vert_\infty}$
192.749	6.53×10^{-35}	2.13×10^{-45}	0.206	8.25×10^{-35}	2.70×10^{-45}	0.323
193.494	5.31×10^{-35}	1.74×10^{-45}	0.198	5.08×10^{-35}	1.66×10^{-45}	0.199
193.947	4.46×10^{-35}	1.47×10^{-45}	0.142	4.43×10^{-35}	1.45×10^{-45}	0.174
202.316	1.46×10^{-34}	4.96×10^{-45}	0.479	4.17×10^{-35}	1.42×10^{-45}	0.170
204.196	1.32×10^{-34}	4.53×10^{-45}	0.438	3.25×10^{-35}	1.11×10^{-45}	0.133
212.556	2.92×10^{-34}	1.03×10^{-44}	1.000	2.36×10^{-34}	8.34×10^{-45}	1.000
214.769	1.62×10^{-34}	5.79×10^{-45}	0.559	4.18×10^{-35}	1.49×10^{-45}	0.179
216.667	1.67×10^{-34}	6.01×10^{-45}	0.581	6.33×10^{-35}	2.27×10^{-45}	0.272

Table 10: Single-Path Approximation Calculations.

λ_L (nm)	State $\|k\rangle$	State $\|f\rangle$	$\sigma_o^{(2)}$ (cm^4)	$\sigma^{(2)}$ $(cm^4 \cdot s)$	$\frac{\sigma^{(2)}}{\|\|\sigma^{(2)}\|\|_\infty}$
192.749	$\|1\rangle$	$\|15\rangle$	4.73×10^{-37}	1.55×10^{-47}	0.016
193.494	$\|1\rangle$	$\|16\rangle$	1.04×10^{-37}	3.40×10^{-48}	0.004
193.947	$\|1\rangle$	$\|17\rangle$	2.01×10^{-37}	6.60×10^{-48}	0.007
202.316	$\|3\rangle$	$\|12\rangle$	1.40×10^{-35}	4.75×10^{-46}	0.496
204.196	$\|3\rangle$	$\|11\rangle$	2.80×10^{-35}	9.57×10^{-46}	1.000
212.556	$\|1\rangle$	$\|5\rangle$	1.72×10^{-35}	6.08×10^{-46}	0.635
214.769	$\|1\rangle$	$\|6\rangle$	8.54×10^{-35}	3.05×10^{-46}	0.318
216.667	$\|1\rangle$	$\|9\rangle$	2.50×10^{-35}	8.98×10^{-46}	0.939

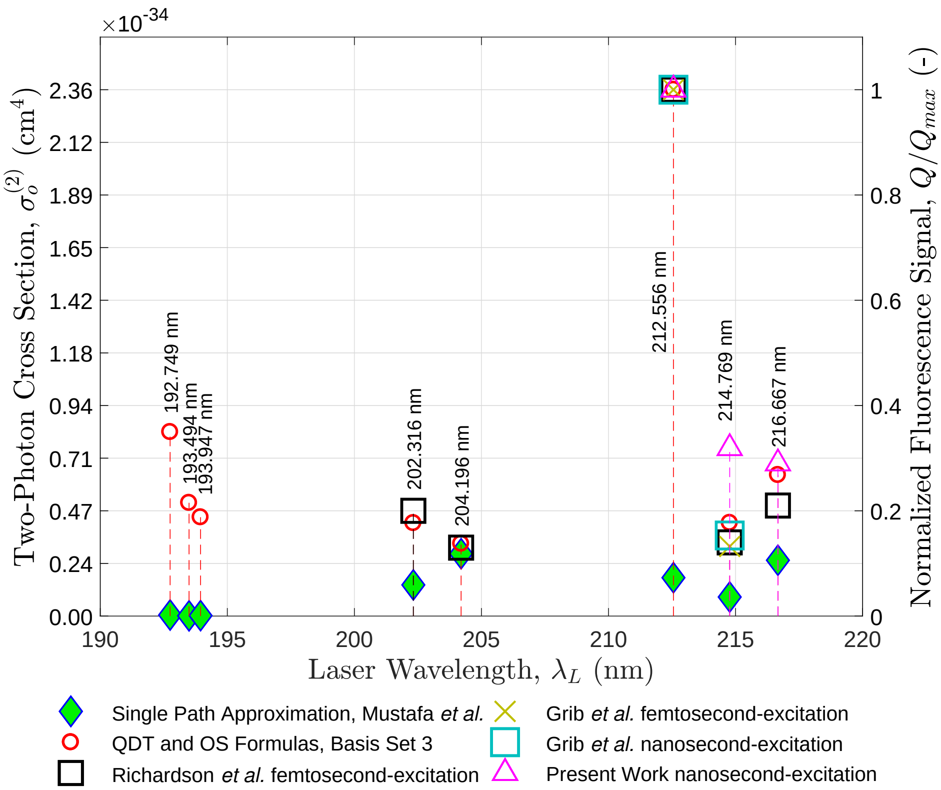

Figure 5: Two-photon excitation cross-sections using basis set 3 as the basis of intermediate states, which included $5s$, $6s$, $7s$, $4d$, $5d$, and $6d$ states. Via quantum-defect theory (QDT) and oscillator strength formulas, cross-sections were calculated and compared to the excitation data of Richardson *et al.*, Grib *et al.*, and our lab. Richardson data was obtained by fs-laser excitation in a 1 bar, 95% Ar/5% gas mixture. Grib data were obtained by both fs-laser and ns-laser excitations in a 1 atm, 77% N_2/33% Kr gas mixture. Our lab data was obtained via ns-laser excitation in 1 torr, 99% N_2/1% Kr gas mixture to minimize collisional effects. Calculated cross-sections and normalized experimental excitation data are listed in Appendix A.

V. Comparison of Two-Photon Cross-section Calculation with Experiment

Cross-section calculations are reported for eight excitation lines (192.749 nm, 193.494 nm, 193.947 nm, 202.316 nm, 204.196 nm, 212.556 nm, 214.769 nm, 216.667 nm) in Tables 7, 8, and 9 for basis sets 1, 2, and 3 respectively. Due to short timescales, these cross-section calculations are then directly compared to

[e]NIST estimated accuracy of Einstein Coefficient. $AAA \leq 0.3\%$, $AA \leq 1\%$, $A \leq 3\%$, $B+ \leq 7\%$, $B \leq 10\%$, $C+ \leq 18\%$, $C \leq 25\%$.

Table 11: Experimental Kr Excitation Signal normalized against 212.556 nm Excitation Signal.

λ_L (nm)	202.316	204.196	212.556	214.769	216.667
Richardson *et al.* fs-excitation	0.20	0.13	1.00	0.14	0.21
Grib *et al.* fs-excitation	(-)	(-)	1.00	0.153	(-)
Grib *et al.* ns-excitation	(-)	(-)	1.00	0.132	(-)
Present Work ns-excitation	(-)	(-)	1.00	0.319	0.290

three sets of excitation spectrum data in Fig. 5 with good agreement. The first experimental data set is from our lab's nanosecond excitation at 212.556 nm, 214.769 nm, and 216.667 nm. Excitation lines at lower wavelengths with the setup are not currently accessible. Additionally, we present the Richardson *et al.*[13] excitation spectrum from a femtosecond excitation at 202.316 nm, 204.196 nm, 212.556 nm, 214.769 nm, and 216.667 nm. This spectrum approximates the impulse/natural response of the Kr atom. Due to the short timescales of excitation of Richardson *et al.*,[13] and due to the closely clustered energies of eight, two-photon excited krypton states, the two-photon cross-section can be compared directly to the fluorescence results. The plotted, relative fluorescence signal magnitudes for 212.556 nm and 214.769 nm excitation of Grib *et al.*[14] also agree with both Richardson *et al.*[13] excitation spectrum and our excitation spectrum, regardless of fs- or ns- laser excitation. Normalized experimental excitation data are listed in Table 11 for all considered data sets. In Fig. 5, comparison is also made to the single-path approximation, whose cross-section values are listed in Table 10. Single-path approximation is unable to reconstruct the experimentally observed excitation spectrum, but it can obtain rough estimates of cross-sections.

The convergence of the summation over the intermediate basis set $|k\rangle$ is shown in tables 7, 8, and 9, which agrees with the convergence criterion of Eq. 13: $n_{max} \leq 7$. The rate of convergence cannot be inferred, but for basis sets 1-3, the Richardson trend is present for the 212.556 nm, 214.769 nm, and 216.667 nm excitation lines.

In Table 9, the calculated cross-section for 214.769 nm excitation is 4.18×10^{-35} cm^4. This cross-section agrees well with the experimentally measured 214.769 nm two-photon cross-section of Dakka *et al.*:[33] $5.2 \pm 2.2 \times 10^{-35}$ cm^4. This validates the order of magnitude and accuracy of calculated cross-sections for basis set 3.

Overall, the comparison of the calculated two-photon cross-sections with the experimental data of multiple research groups is good for lines between 200-220 nm. Cross-sections for lines between 190-200 nm are predictions calculated by the method described within this paper. The multi-path, finite basis approximation of the two-photon transition matrix element, $M_{fg}^{(2)}$, generated context for each calculated excitation cross-section. From a first order perturbation calculation, an entire excitation spectrum was constructed with sufficient accuracy. This paper improved the effectiveness of first order perturbation theory for multiphoton processes beyond a mere order of magnitude calculation.

VI. Experimental Setup

The experiments were performed in a test cell that had optical ports for a laser and camera. The cell was maintained at room temperature. Two quiescent gas mixtures were used, 99% N_2/1% Kr and 75% N_2/20% O_2/5% Kr. The pressure was varied from 1-100 torr in the 99% N_2/1% Kr mixture and from 1-50 torr in the 75% N_2/5% Kr/20% O_2 mixture. The maximum pressure for the 75% N_2/5% Kr/20% O_2 mixture is lower because beyond 50 torr the signal was entirely quenched owing to the presence of O_2 at the current laser power.

A frequency-doubled Quanta Ray Pro-350 Nd:YAG laser pumping a frequency tripled Sirah PrecisionScan Dye Laser (DCM dye, DMSO solvent) is the approach used for nanosecond excitation in this work. A schematic of the optical setup is shown in Fig. 6. The Nd:YAG laser pumps the dye laser with 1000 mJ/pulse at a wavelength of 532 nm. The dye laser is tuned to output a 637.67/644.31/650.01 nm beam and frequency tripling (Sirah THU 205) of the dye-laser output results in a 212.56/214.77/216.67 nm beam, with 3 mJ energy, 1350 MHz linewidth and 7 ns pulsewidth at a repetition rate of 10 Hz. The write beam was focused into the test section with a 200 mm focal-length, fused-silica lens. The beam fluence and spectral intensity

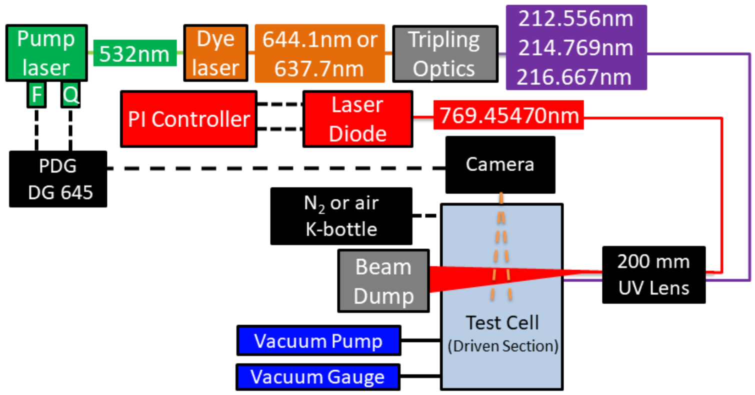

Figure 6: Schematic of experimental setup. PDG refers to pulse delay generator.

at the waist were 1.28×10^4 J/cm^2 and 1.35×10^3 W/(cm^2 Hz), respectively.

Excitation of the Kr metastable state was accomplished by a continuous wave 2.65 W Toptica TA Pro Laser diode, which outputted a $\lambda_L = 769.45470$ nm beam with a waist of 3.28 mm. The diode wavelength was regulated by feedback control on the piezoelectric voltage input of the DCL Pro, which powered the diode. The feedback and control signals were provided by a WS7-4150 Wavelength Meter, which measured the wavelength of the diode to 0.00001 nm precision and implemented the PI-control law. Online tuning obtained PI-control gains. The sampling rate of the wavelength meter was set between 90-100 ms. In order to prevent saturation of the piezoelectric voltage, manual tuning of the diode diffraction grating via a 2.5 mm Allen key was used to bring the diode within ± 0.02 nm from the desired operating wavelength, prior to the implementation of the control law.

The intensified CCD camera used for all experiments is a Princeton Instruments PIMAX-4 (PM4-1024i-HR-FG-18-P46-CM) with a Nikon NIKKOR 24-85mm f/2.8-4D lens in "macro" mode and positioned approximately 200 mm from the write/read location. The camera gate opens once immediately after the write laser pulse, for 50 ns to capture the fluorescence from transitions C, D, M, N, O in Fig. 1. The raw image from the camera was processed using a Gaussian peak finding algorithm from O'Haver[53] to quantify the value of the peak in each row of the fluorescence image. The final value of the signal that is reported is the average value of the peaks in the rows closest to the focus of the tagged line.

VII. Experimental Results

In Figs. 7 and 8, experimental data is presented for each stage of Kr laser-induced fluorescence (LIF) to highlight physical features that would otherwise be difficult to model. One example would be the signal contribution of radiative cascade in a cold, partially ionized Kr plasma and the relative SNR of laser excitation schemes at different times Δt after the rising edge of the laser pulse, both with and without an 800 nm highpass filter.

In the fluorescence vs. pressure curves shown in Figs. 7 and 8, the 212.556 nm excitation line has the greatest fluorescence of the lines considered at zero time delay, indicating its optimality for Kr-PLIF. Also evident from Figs. 7 and 8 is that 216 nm is the best excitation line for KTV with the read excitation performed with a CW laser diode.

Time-dependent phenomena such as pressure-dependent collisional de-excitation and collision-driven electron cooling[54] become important and affect the fluorescence signal, notably more in air than in N_2.

VIII. Conclusions

This paper presents multi-path, two-photon excitation cross-section calculations for krypton that compare well to experiment for lines between 200-220 nm, as shown in fig. 5. Cross-sections were also calculated for excitation wavelengths lying between 190-200 nm.

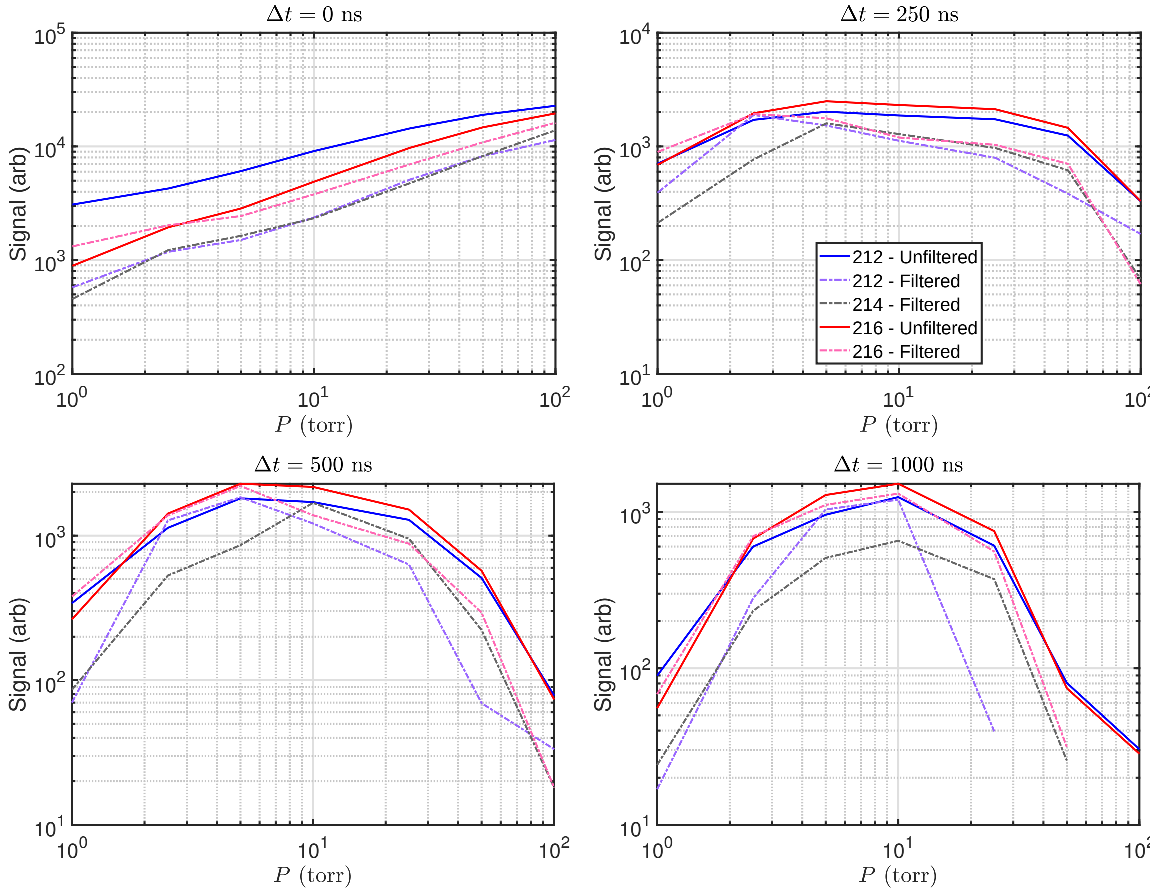

Figure 7: Kr Fluorescence signal in 99% N_2/1% Kr at Time Δt after dye laser pulse: (*Top Left*) 0 ns, (*Top Right*) 250 ns, (*Bottom Left*) 500 ns, and (*Bottom Right*) 1000 ns. This is two-laser excitation. A 769.4547 nm continuous diode was used to excite metastable Kr. The filter used was an 800 highpass filter.

To make these calculations, a hybrid method was used, consisting of oscillator-strengths, and where those are unlisted in the NIST data, QDT, to evaluate reduced matrix elements $\langle \vec{r}\,\rangle$ and purely radial matrix elements $\langle r \rangle$. QDT was used to (1) construct radial wave functions for excited Kr states and (2) predict the sign of tabulated and calculated oscillator strengths from NIST. Including the transition pathways unlisted in the NIST data was key to increasing the accuracy of the calculation. These pathways were constructed from a finite basis of states (listed in Table 5) consisting of $4p$, $5s$, $6s$, $7s$, $5p$, $6p$, $4d$, $5d$, and $6d$ orbitals.

Most importantly, this work provides a fundamental physical understanding in identifying the optimal Kr fluorescence excitation line (i.e., Kr-PLIF or KTV). This paper resolved the fine structure nature of eight $5p$ and $6p$ Kr states produced by two-photon excitation. From this work and the successful comparison to experiment from our lab and those in the literature, we conclude that the optimal line is 212.556 nm for Kr-PLIF and single-laser KTV. For KTV where the read step in performed with a CW laser diode, the 216.667 nm write-laser excitation is optimal.

Acknowledgments

Mustafa and Parziale were supported by AFOSR Young Investigator Program Grant FA9550-16-1-0262, and equipment for this work was supported by AFOSR DURIP Grant FA9550-15-1-0325; Ivett Leyva of AFOSR is the Program Manager for both grants. Support was also provided by U.S. Air Force grant (USAF) (FA9101-17-P-0094). David Shekhtman was supported by the ONR Grants N00014-19-1-2523, N00014-20-1-2549, and N00014-20-1-2637 for which Eric Marineau is the Program Manager. We also acknowledge the helpful consultation of Professors Vladimir Lukic and Kevin Connington on theoretical and numerical matters, such as the evaluation of reduced matrix elements and the use of the spectral-shifted inverse power

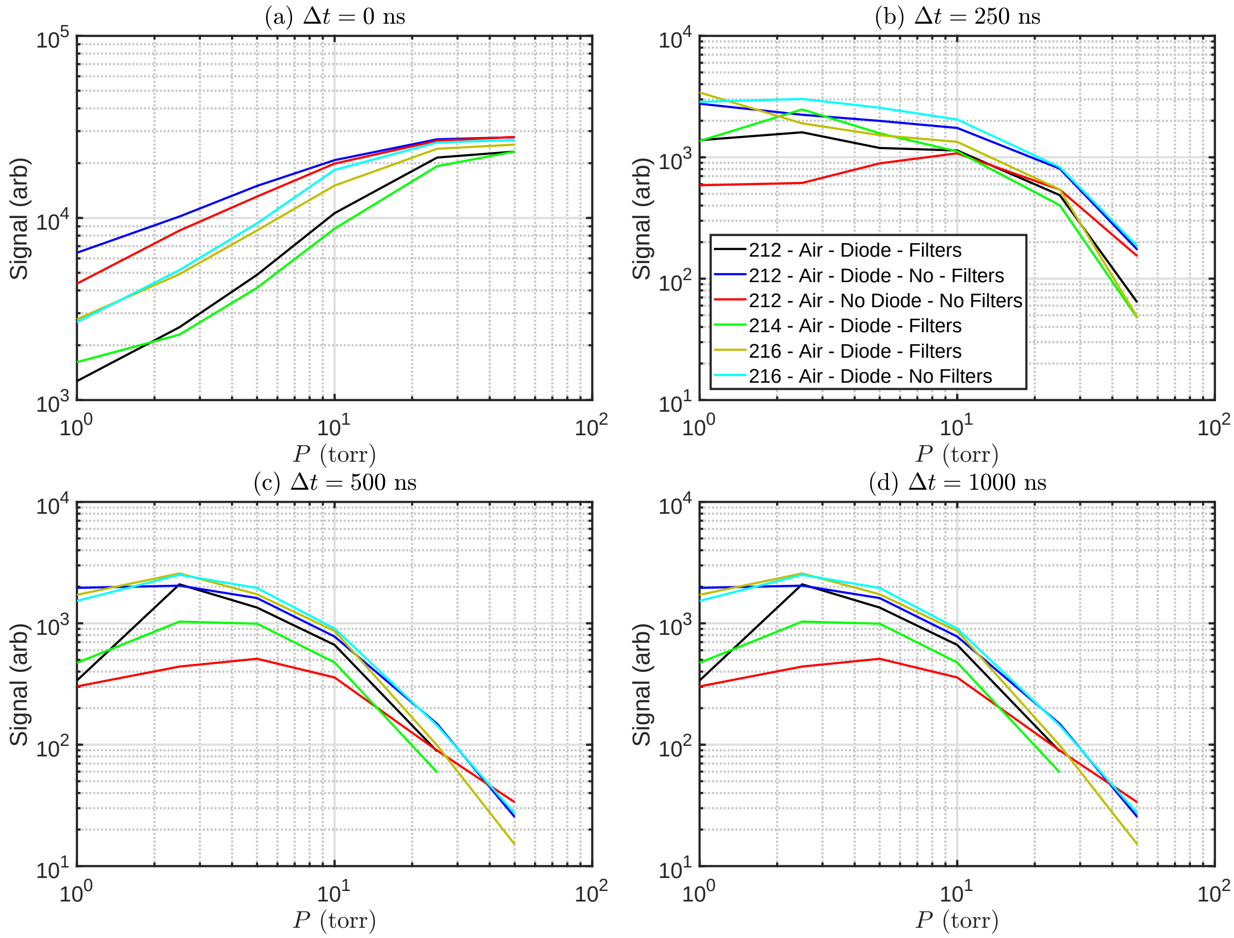

Figure 8: Kr Fluorescence Signal in 5%-Kr, 20%-O_2, and 75%-N_2 at Time Δt after laser pulse. (a) 0 ns, (b) 250 ns, (c) 500 ns, and (d) 1000 ns.

method in the Hartree-Fock method.

References

[1]Danehy, P. M., Weisberger, J., Johansen, C., Reese, D., Fahringer, T., Parziale, N. J., Dedic, C., Estevadeordal, J., and Cruden, B. A., "Non-Intrusive Measurement Techniques for Flow Characterization of Hypersonic Wind Tunnels," *Flow Characterization and Modeling of Hypersonic Wind Tunnels (NATO Science and Technology Organization Lecture Series STO-AVT 325)*, NF1676L-31725 - Von Karman Institute, Brussels, Belgium, December 3-5 2018.

[2]Whitehead, C. A., Cannon, B. D., and Wacker, J. F., "Trace detection of krypton using laser-induced fluorescence," *Applied Optics*, Vol. 34, No. 18, 1995, pp. 3250–3256. doi: 10.1364/AO.34.003250.

[3]Narayanaswamy, V., Burns, R., and Clemens, N. T., "Kr-PLIF for scalar imaging in supersonic flows," *Optics Letters*, Vol. 36, No. 21, 2011, pp. 4185–4187. doi: 10.1364/OL.36.004185.

[4]Hsu, A. G., Narayanaswamy, V., Clemens, N. T., and Frank, J. H., "Mixture fraction imaging in turbulent non-premixed flames with two-photon LIF of krypton," *Proceedings of the Combustion Institute*, Vol. 33, No. 1, 2011, pp. 759–766. doi: 10.1016/j.proci.2010.06.051.

[5]Buxton, O. R. H., Burns, R. A., and Clemens, N. T., "Simultaneous Krypton PLIF, LII and PIV Measurements in a Sooting Jet Flame," *Proceedings of 51st AIAA Aerospace Sciences Meeting including the New Horizons Forum and Aerospace Exposition*, AIAA-2013-0479, Grapevine, Texas, 2013. doi: 10.2514/6.2013-479.

[6]Park, O., Burns, R. A., Buxton, O. H. R., and Clemens, N. T., "Mixture fraction, soot volume fraction, and velocity imaging in the soot-inception region of a turbulent non-premixed jet flame," *Proceedings of the Combustion Institute*, Vol. 36, No. 1, 2017, pp. 899–907. doi: 10.1016/j.proci.2016.08.048.

[7]Zelenak, D. and Narayanaswamy, V., "Composition-independent mean temperature measurements in laminar diffusion flames using spectral lineshape information," *Experiments in Fluids*, Vol. 58, No. 10, 2017, pp. 147. doi: 10.1007/s00348-017-2430-y.

[8]Sahoo, A. and Narayanaswamy, V., "Two-dimensional temperature field imaging in laminar sooting flames using a two-line

Kr PLIF approach," *Applied Physics B*, Vol. 125, No. 9, 2019, pp. 168. doi: 10.1007/s00340-019-7280-2.

[9]Zelenak, D. and Narayanaswamy, V., "Demonstration of a two-line Kr PLIF thermometry technique for gaseous combustion applications," *Optics Letters*, Vol. 44, No. 2, 2019, pp. 367–370. doi: 10.1364/OL.44.000367.

[10]Niemi, K., Schulz-Von Der Gathen, V., and Döbele, H. F., "Absolute calibration of atomic density measurements by laser-induced fluorescence spectroscopy with two-photon excitation," *Journal of Physics D: Applied Physics*, Vol. 34, No. 15, 2001, pp. 2330. doi: 10.1088/0022-3727/34/15/312.

[11]Schmidt, J. B., Roy, S., Kulatilaka, W. D., Shkurenkov, I., Adamovich, I. V., Lempert, W. R., and Gord, J. R., "Femtosecond, two-photon-absorption, laser-induced-fluorescence (fs-TALIF) imaging of atomic hydrogen and oxygen in non-equilibrium plasmas," *Journal of Physics D: Applied Physics*, Vol. 50, No. 1, 2016, pp. 015204. doi: 10.1088/1361-6463/50/1/015204.

[12]Wang, Y., Capps, C., and Kulatilaka, W. D., "Femtosecond two-photon laser-induced fluorescence of krypton for high-speed flow imaging," *Optics letters*, Vol. 42, No. 4, 2017, pp. 711–714. doi: 10.1364/OL.42.000711.

[13]Richardson, D. R., Jiang, N., Stauffer, H. U., Kearney, S. P., Roy, S., and Gord, J. R., "Mixture-fraction imaging at 1 kHz using femtosecond laser-induced fluorescence of krypton," *Optics Letters*, Vol. 42, No. 17, 2017, pp. 3498–3501. doi: 10.1364/OL.42.003498.

[14]Grib, S. W., Hsu, P. S., Stauffer, H. U., Carter, C. D., and Roy, S., "Comparison of femtosecond and nanosecond two-photon-absorption laser-induced fluorescence of krypton," *Applied Optics*, Vol. 58, No. 27, 2019, pp. 7621–7627. doi: 10.1364/AO.58.007621.

[15]Grib, S. W., Hsu, P. S., Jiang, N., Felver, J. J., Schumaker, S. A., Carter, C. D., and Roy, S., "100 kHz krypton planar laser-induced fluorescence imaging," *Optics Letters*, Vol. 45, No. 14, 2020, pp. 3832–3835. doi: 10.1364/OL.395389.

[16]Mills, J. L., Sukenik, C. I., and Balla, R. J., "Hypersonic Wake Diagnostics Using Laser Induced Fluorescence Techniques," *Proceedings of 42nd AIAA Plasmadynamics and Lasers Conference*, AIAA 2011-3459, Honolulu, Hawaii, 2011. doi: 10.2514/6.2011-3459.

[17]Balla, R. J. and Everhart, J. L., "Rayleigh Scattering Density Measurements, Cluster Theory, and Nucleation Calculations at Mach 10," *AIAA Journal*, Vol. 50, No. 3, 2012, pp. 698–707. doi: 10.2514/1.J051334.

[18]Parziale, N. J., Smith, M. S., and Marineau, E. C., "Krypton tagging velocimetry of an underexpanded jet," *Applied Optics*, Vol. 54, No. 16, 2015, pp. 5094–5101. doi: 10.1364/AO.54.005094.

[19]Zahradka, D., Parziale, N. J., Smith, M. S., and Marineau, E. C., "Krypton tagging velocimetry in a turbulent Mach 2.7 boundary layer," *Experiments in Fluids*, Vol. 57, 2016, pp. 62. doi: 10.1007/s00348-016-2148-2.

[20]Mustafa, M. A., Hunt, M. B., Parziale, N. J., Smith, M. S., and Marineau, E. C., "Krypton Tagging Velocimetry (KTV) Investigation of Shock-Wave/Turbulent Boundary-Layer Interaction," *Proceedings of AIAA SciTech 2017*, AIAA-2017-0025, Grapevine, Texas, 9-13 January 2017. doi: 10.2514/6.2017-0025.

[21]Mustafa, M. A., , and Parziale, N. J., "Krypton Tagging Velocimetry in the Stevens Shock Tube," *Proceedings of 33rd AIAA Aerodynamic Measurement Technology and Ground Testing Conference*, AIAA-2017-3897, Denver, Colorado, 5-9 June 2017. doi: 10.2514/6.2017-3897.

[22]Mustafa, M. A., Parziale, N. J., Smith, M. S., and Marineau, E. C., "Nonintrusive Freestream Velocity Measurement in a Large-Scale Hypersonic Wind Tunnel," *AIAA Journal*, Vol. 55, No. 10, 2017, pp. 3611–3616. doi: 10.2514/1.J056177.

[23]Mustafa, M. A., Parziale, N. J., Smith, M. S., and Marineau, E. C., "Two-Dimensional Krypton Tagging Velocimetry (KTV-2D) Investigation of Shock-Wave/Turbulent Boundary-Layer Interaction," *Proceedings of AIAA SciTech 2018*, AIAA-2018-1771, Kissimmee, Florida, 8-12 January 2018. doi: 10.2514/6.2018-1771.

[24]Mustafa, M. A., Parziale, N. J., Smith, M. S., and Marineau, E. C., "Amplification and structure of streamwise-velocity fluctuations in four shock-wave/turbulent boundary-layer interactions," *Proceedings of AIAA Aviation 2018*, AIAA-2018-3704, Atlanta, Georgia, 25-29 June 2018. doi: 10.2514/6.2018-3704.

[25]Mustafa, M. A., Parziale, N. J., Smith, M. S., and Marineau, E. C., "Amplification and structure of streamwise-velocity fluctuations in compression-corner shock-wave/turbulent boundary-layer interactions," *Journal of Fluid Mechanics*, Vol. 863, 2019, pp. 1091–1122. doi: 10.1017/jfm.2018.1029.

[26]Mustafa, M. A. and Parziale, N. J., "Simplified read schemes for krypton tagging velocimetry in N_2 and air," *Optics Letters*, Vol. 43, No. 12, 2018, pp. 2909–2912. doi: 10.1364/OL.43.002909.

[27]Mustafa, M. A., Shekhtman, D., and Parziale, N. J., "Single-Laser Krypton Tagging Velocimetry Investigation of Supersonic Air and N_2 Boundary-Layer Flows over a Hollow Cylinder in a Shock Tube," *Physical Review Applied*, Vol. 11, No. 6, 2019, pp. 064013. doi: 10.1103/PhysRevApplied.11.064013.

[28]Shekhtman, D., Mustafa, M. A., and Parziale, N. J., "Two-photon cross-section calculations for krypton in the 190-220 nm range," *Applied Optics*, Vol. 59, No. 34, 2020, pp. 10826–10837. doi: 10.1364/AO.410806.

[29]Fonseca, V. and Campos, J., "Lifetimes of Some Levels Belonging to the $4p^5 5p$ and $4p^5 6p$ Configurations of Kr $_I$," *Physical Review A*, Vol. 17, No. 3, 1978, pp. 1080–1082. doi: 10.1103/PhysRevA.17.1080.

[30]Saito, N., Oishi, Y., Miyazaki, K., K., O., Nakamura, J., Louchev, O., Iwasaki, M., and Wada, S., "High-efficiency generation of pulsed Lyman-α radiation by resonant laser wave mixing in low pressure Kr-Ar mixture," *Optics Express*, Vol. 24, No. 7, 2016, pp. 215–386. doi: 10.1364/OE.24.007566.

[31]Miller, J. C., "Two-photon resonant multiphoton ionization and stimulated emission in krypton and xenon," *Physical Review A*, Vol. 40, 1989, pp. 6969–6976. doi: 10.1103/PhysRevA.40.6969.

[32]Shiu, Y. and Biondi, M. A., "Dissociative recombination in krypton: Dependence of the total rate coefficient and excited-state production on electron temperature," *Physical Review Applied*, Vol. 16, Nov 1977, pp. 1817–1820. doi: 10.1103/PhysRevA.16.1817.

[33]Dakka, M. A., Tsiminis, G., Glover, R. D., Perrella, C., Moffatt, J., Spooner, N. A., Sang, R. T., Light, P. S., and Luiten, A. N., "Laser-Based Metastable Krypton Generation," *Phys. Rev. Lett.*, Vol. 121, Aug 2018, pp. 093201. doi: 10.1103/PhysRevLett.121.093201.

[34]Eckbreth, A. C., *Laser Diagnostics for Combustion Temperature and Species*, Gordon and Breach Publications, 2nd ed., 1996.

[35]Khambatta, N. M., Oertel, J. A., Silk, R., Radziemski, L. J., and Mack, J. M., "Absolute excited state and ion densities from two-and three-photon processes in some 6p levels of atomic krypton," *Journal of Applied Physics*, Vol. 64, No. 10, 1988, pp. 4809–4814. doi: 10.1063/1.341226.

[36]Lambropoulos, P., "Topics on Multiphoton Processes in Atoms," *Advances in Atomic and Molecular Physics*, Vol. 12, 1976, pp. 87–164. doi: 10.1016/S0065-2199(08)60043-3.

[37]Khambatta, N. M., Radziemski, L. J., and Dixit, S. N., "Upper bound for a three-photon excitation cross section in atomic argon in the ultraviolet regime," *Physical Review A*, Vol. 39, 1989, pp. 3842–3845. doi: 10.1103/PhysRevA.39.3842.

[38]Hillborn, R. C., "Einstein Coefficients, Cross Sections, f Values, Dipole Moments, and All That," *Am. J. of Phys.*, Vol. 50, No. 11, 1981, pp. 982–986. doi: 10.1119/1.12937.

[39]Bokor, J., Zavelovich, J. Y., and Rhodes, C. K., "Multiphoton ultraviolet spectroscopy of some 6p levels in krypton," *Physical Review A*, Vol. 21, No. 5, 1980, pp. 1453–1459. doi: 10.1103/PhysRevA.21.1453.

[40]Clementi, E. and Roetti, C., "Roothaan-Hartree-Fock Atomic Wavefunctions: Basis Functions and their Coefficients for Ground and Certain Excited States of Neutral and Ionized Atoms, $Z \leq 54$," *Atomic Data and Nuclear Data Tables*, Vol. 14, No. 3-4, 1974, pp. 177–478. doi: 10.1016/S0092-640X(74)80016-1.

[41]Kramida, A., Yu. Ralchenko, Reader, J., and and NIST ASD Team, NIST Atomic Spectra Database (ver. 5.5.6), [Online]. Available: `https://physics.nist.gov/asd` [2020, April 16]. National Institute of Standards and Technology, Gaithersburg, MD., 2020.

[42]Bethe, H. A. and Salpeter, E. E., *Quantum Mechanics of One- and Two-Electron Atoms*, Springer-Verlag Academic Press, Inc., 1957.

[43]Liboff, R. L., *Introductory Quantum Mechanics*, Pearson Education, 4th ed., 2003.

[44]Park, C., *Nonequilibrium Hypersonic Aerothermodynamics*, John Wiley & Sons, 1st ed., 1990.

[45]Louchev, O. A., Saito, N., Miyazaki, K., Okamura, K., Nakamura, J., Iwasaki, M., and Wada, S., "Photoionization Pathways and Thresholds in Generation of Lyman-α Radiation by Resonant Four-Wave Mixing in Kr-Ar mixture," *AIP Advances*, Vol. 6, No. 095018, 2016, pp. 1–10. doi: 10.1063/1.4963303.

[46]Demtröder, W., *Atoms, Molecules, and Photons: An Introduction to Atomic-, Molecular, and Quantum-Physics*, Springer, 2006.

[47]Messiah, A., *Quantum Mechanics*, Dover Publications, Inc., 2014.

[48]Kostelecký, V. A. and Nieto, M. M., "Analytical Wave Functions for Quantum-Defect Theory," *Physical Review A.*, Vol. 32, No. 6, 1985, pp. 3243–3246. doi: 10.1103/physreva.32.3243.

[49]Bebb, H. B. and Gold, A., "Multiphoton Ionization of Hydrogen and Rare-Gas Atoms," *Physical Review*, Vol. 143, No. 1, 1966, pp. 1–24. doi: 10.1103/PhysRev.143.1.

[50]McGuire, E. J., "Green's-function approach to nonresonance multiphoton absorption in the alkali-metal atoms," *Physical Review A.*, Vol. 23, No. 1, 1981, pp. 186–200. doi: 10.1103/PhysRevA.23.186.

[51]McGuire, E. J., "Two- and three-photon ionization in the noble gases," *Physical Review A.*, Vol. 24, No. 2, 1981, pp. 835–848. doi: 10.1103/PhysRevA.24.835.

[52]Miller, D. A. B., *Quantum Mechanics for Engineers and Scientists*, Cambridge University Press, 2008.

[53]O'Haver, T., *A Pragmatic Introduction to Signal Processing*, University of Maryland at College Park, 1997.

[54]Mariotti, D., Shimizu, Y., Sasaki, T., and Koshizaki, N., "Gas Temperature and Electron Temperature Measurements by Emission Spectroscopy for an Atmospherica Microplasma," *Journal of Applied Physics*, Vol. 101, No. 013307, 2007, pp. 1–8. doi: 10.1063/1.2409318.

Appendix A: An Intermediate State in Two-Photon Excitation

This section is included to discuss the nature of intermediate states $|i\rangle$ and why it is valid to assume a basis of normalized eigenstates $|k\rangle$. Consider intermediate state $|i\rangle$ composed of a linear combination of states $|k\rangle$, weighted by coefficients c_{ik}:

$$|i\rangle = \sum_k c_{ik} |k\rangle . \tag{43}$$

A physical property that intermediate state $|i\rangle$ must satisfy is expected energy:

$$E_g + \hbar\omega_L = \langle i| \hat{H} |i\rangle , \tag{44}$$

where $\hat{H}$ is the Hamiltonian operator. Another property that must be satisfied is normalization:

$$1 = \langle i|i\rangle = \sum_{k,k'} \delta_{k,k'} c_{ki} c_{ik'} \langle k|k'\rangle = \sum_k c_{ki} c_{ik}. \tag{45}$$

Let us revisit equation eq. (19) but perform the summation in the physical intermediate basis $|i\rangle$:

$$M_{fg}^{(2)} = \sum_{i=g}^{N} D_{fi} G_{ii} D_{ig}. \tag{46}$$

Applying eqs. (43) and (45),

$$M_{fg}^{(2)} = \sum_{k=g}^{N} \sum_{k'=g}^{N} \sum_{i=g}^{N} \delta_{kk'} D_{fi} (c_{ik} c_{ki}) G_{ii} (c_{ik'} c_{k'i}) D_{ig}. \tag{47}$$

Since $|i\rangle$ is expressed by basis set $|k\rangle$, c_{ik} is a diagonal matrix and $k = i$. Hence,

$$\begin{aligned} M_{fg}^{(2)} &= \sum_{k=g}^{N} D_{fk} (c_{kk} c_{kk}) G_{kk} (c_{kk} c_{kk}) D_{kg} \\ &= \sum_{k=g}^{N} D_{fk} G_{kk} D_{kg} = \hat{e}_f D G D \hat{e}_g. \end{aligned} \tag{48}$$

By recovering the result of eq. (19), basis set $|k\rangle$ correctly describes the intermediate state of two-photon excitation. For intermediate states, it is not necessary to solve for a mixed state $|i\rangle$, i.e. the sum of linearly weighted states described in eq. (45). Basis set $|k\rangle$ serves perfectly well, essentially due to the tensor properties of the two-photon transition matrix M^2.

Appendix B: Determination of Weighting parameter w_t

The probability of a dipole transition occurring between two degenerate states in an isotropic electric field is $1/w_t$. Thus, the weight on a single dipole moment is $1/\sqrt{w_t}$ because the probability rate of a dipole transition is proportional to the square of the dipole moment. This section also showcases the symmetry of the 3j-Wigner symbol (the Clebsch-Gordan coefficient) due to the even parity of the sum, $J_i + 1 + J_j$, which represents the sum of the first row. This further cements the symmetry of the dipole matrix D. Matrix D is indeed a rank 2 tensor.

Case 1a: Transitions with $l_j = 0$ to $l_i = 1$

$$\begin{pmatrix} 1 & 1 & 0 \\ 0 & 0 & 0 \end{pmatrix} = -\frac{1}{\sqrt{3}} \quad \begin{pmatrix} 1 & 1 & 0 \\ -1 & 1 & 0 \end{pmatrix} = \frac{1}{\sqrt{3}} \quad \begin{pmatrix} 1 & 1 & 0 \\ 1 & -1 & 0 \end{pmatrix} = \frac{1}{\sqrt{3}} \tag{49}$$

In this case, there are three possible transitions: $w_t = 3$. The 2-norm is 1.

Case 1b: Transitions with $l_j = 1$ to $l_i = 0$

$$\begin{pmatrix} 0 & 1 & 1 \\ 0 & 0 & 0 \end{pmatrix} = -\frac{1}{\sqrt{3}} \quad \begin{pmatrix} 0 & 1 & 1 \\ 0 & 1 & -1 \end{pmatrix} = \frac{1}{\sqrt{3}} \quad \begin{pmatrix} 0 & 1 & 1 \\ 0 & -1 & 1 \end{pmatrix} = \frac{1}{\sqrt{3}} \tag{50}$$

This case also has three possible transitions: $w_t = 3$. The 2-norm is 1.

Case 2a: Transitions with $l_j = 1$ to $l_i = 2$

$$\begin{gathered} \begin{pmatrix} 2 & 1 & 1 \\ 0 & 0 & 0 \end{pmatrix} = \sqrt{\frac{2}{15}} \quad \begin{pmatrix} 2 & 1 & 1 \\ 0 & 1 & -1 \end{pmatrix} = \frac{1}{\sqrt{30}} \quad \begin{pmatrix} 2 & 1 & 1 \\ 0 & -1 & 1 \end{pmatrix} = \frac{1}{\sqrt{30}} \\ \begin{pmatrix} 2 & 1 & 1 \\ -1 & 1 & 0 \end{pmatrix} = -\frac{1}{\sqrt{10}} \quad \begin{pmatrix} 2 & 1 & 1 \\ -1 & 0 & 1 \end{pmatrix} = -\frac{1}{\sqrt{10}} \quad \begin{pmatrix} 2 & 1 & 1 \\ 1 & -1 & 0 \end{pmatrix} = -\frac{1}{\sqrt{10}} \\ \begin{pmatrix} 2 & 1 & 1 \\ 1 & 0 & -1 \end{pmatrix} = -\frac{1}{\sqrt{10}} \quad \begin{pmatrix} 2 & 1 & 1 \\ -2 & 1 & 1 \end{pmatrix} = \frac{1}{\sqrt{5}} \quad \begin{pmatrix} 2 & 1 & 1 \\ 2 & -1 & -1 \end{pmatrix} = \frac{1}{\sqrt{5}} \end{gathered} \tag{51}$$

This case has nine possible transitions: $w_t = 9$. The 2-norm is 1.

Case 2b: Transitions with $l_j = 2$ to $l_i = 1$

$$\begin{gathered} \begin{pmatrix} 1 & 1 & 2 \\ 0 & 0 & 0 \end{pmatrix} = \sqrt{\frac{2}{15}} \quad \begin{pmatrix} 1 & 1 & 2 \\ -1 & 1 & 0 \end{pmatrix} = \frac{1}{\sqrt{30}} \quad \begin{pmatrix} 1 & 1 & 2 \\ 1 & -1 & 0 \end{pmatrix} = \frac{1}{\sqrt{30}} \\ \begin{pmatrix} 1 & 1 & 2 \\ 0 & 1 & -1 \end{pmatrix} = -\frac{1}{\sqrt{10}} \quad \begin{pmatrix} 1 & 1 & 2 \\ 0 & -1 & 1 \end{pmatrix} = -\frac{1}{\sqrt{10}} \quad \begin{pmatrix} 1 & 1 & 2 \\ 1 & 0 & -1 \end{pmatrix} = -\frac{1}{\sqrt{10}} \\ \begin{pmatrix} 1 & 1 & 2 \\ -1 & 0 & 1 \end{pmatrix} = -\frac{1}{\sqrt{10}} \quad \begin{pmatrix} 1 & 1 & 2 \\ 1 & 1 & -2 \end{pmatrix} = \frac{1}{\sqrt{5}} \quad \begin{pmatrix} 1 & 1 & 2 \\ -1 & -1 & 2 \end{pmatrix} = \frac{1}{\sqrt{5}} \end{gathered} \tag{52}$$

This case also has nine possible transitions: $w_t = 9$. The 2-norm is 1.